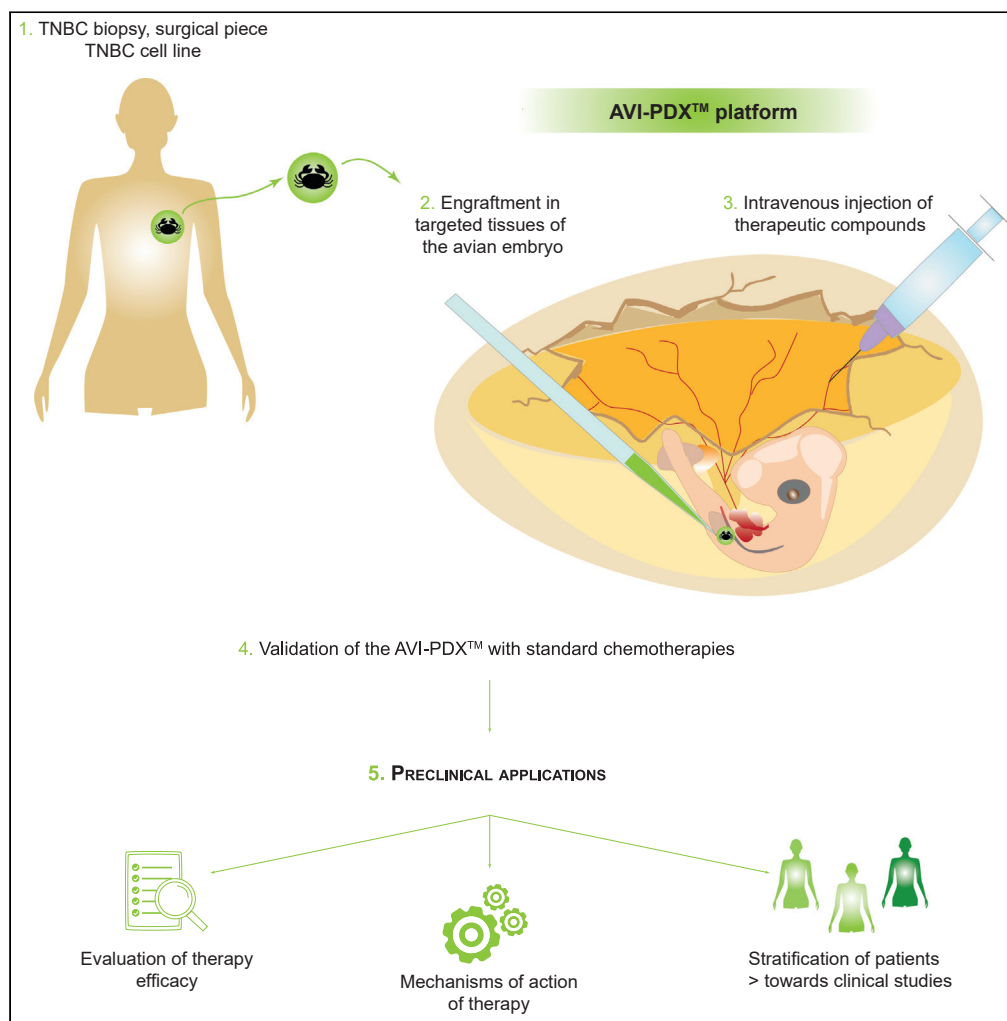


Article

# An avian embryo patient-derived xenograft model for preclinical studies of human breast cancers



Loraine Jarrosson,  
Clélia  
Costechareyre,  
Fanny Gallix, ...,  
Karine Aguéra,  
Céline Delloye-  
Bourgeois, Valérie  
Castellani

celine.delloye@univ-lyon1.fr  
(C.D.-B.)  
valerie.castellani@univ-lyon1.fr  
(V.C.)

Highlights

Human TNBC cells  
implanted in the avian  
embryo survive and  
efficiently form tumors

Anti-tumoral therapies  
intravenously injected are  
assessed by 3D imaging

Post-graft large-scale  
analyses allow studying  
the mechanism of action  
of drugs

The AVI-PDX allows  
preclinical evaluation of  
therapies and patient  
stratification

Jarrosson et al., iScience 24,  
103423  
December 17, 2021 © 2021  
The Authors.  
[https://doi.org/10.1016/  
j.isci.2021.103423](https://doi.org/10.1016/j.isci.2021.103423)



## Article

## An avian embryo patient-derived xenograft model for preclinical studies of human breast cancers

Loraine Jarrosson,<sup>1,5</sup> Clélia Costechareyre,<sup>1,5</sup> Fanny Gallix,<sup>2</sup> Séverine Ciré,<sup>2</sup> Fabien Gay,<sup>2</sup> Olivier Imbaud,<sup>3</sup> Romain Teinturier,<sup>1</sup> Elisabetta Marangoni,<sup>4</sup> Karine Aguéra,<sup>2</sup> Céline Delloye-Bourgeois,<sup>1,3,6,\*</sup> and Valérie Castellani<sup>1,3,6,7,\*</sup>

## SUMMARY

**Lack of preclinical patient-derived xenograft cancer models in which to conduct large-scale molecular studies seriously impairs the development of effective personalized therapies. We report here an *in vivo* concept consisting of implanting human tumor cells in targeted tissues of an avian embryo, delivering therapeutics, evaluating their efficacy by measuring tumors using light sheet confocal microscopy, and conducting large-scale RNA-seq analysis to characterize therapeutic-induced changes in gene expression. The model was established to recapitulate triple-negative breast cancer (TNBC) and validated using TNBC standards of care and an investigational therapeutic agent.**

## INTRODUCTION

The creation of innovative animal models recapitulating patient tumors as closely as possible is crucial for better understanding various types of cancer and for the development of novel therapies. Existing models struggle to establish tumors from patient biopsies in living organisms that also allow for large-scale molecular analysis. Patient-derived xenografts (PDXs) in mouse have represented a breakthrough in cancer models that considerably advanced our knowledge (Dobrolecki et al., 2016). Nevertheless, they suffer from a high degree of tumor intake variability, long and variable timing of tumor growth and engraftment modality classically under the skin, thus in a context not recapitulating the tumor microenvironment (Shi et al., 2020). All these challenges prevent the use of such models in extensive large-scale studies comparing functional responses of single patient tumors to multiple treatment regimens and correlation with specific molecular signatures.

Additionally, such limitations of existing preclinical models curtail the investigation of molecular and therapy-response heterogeneity among patients suffering from the same types of cancers, which investigations would otherwise usher in the development of personalized medicine. Patients would thus benefit substantially from paradigms that afford rapid prediction of their responsiveness or resistance to proposed therapies. This is of central interest for those suffering from cancers with poor outcomes, for which the choice of treatment regimens is particularly complex and fraught with risk.

Breast cancer is the second leading cause of death in women worldwide. The triple-negative breast cancer (TNBC) subtype represents 10%–15% of all diagnosed breast cancers and has the poorest prognosis with a median overall survival for metastasized patients of approximately 18 months (Hwang et al., 2019; Mehanna et al., 2019). TNBC usually appears as a high-grade ductal carcinoma, defined by the lack of expression of estrogen receptor (ER), progesterone receptor, and HER2 receptor, hence the term “triple negative,” and often accompanied by distant metastases. Extensive molecular profiling refined the classification of the different breast cancer subtypes, revealing heterogeneity reflected by six different molecular profiles (Lehmann et al., 2011). Tumor sequencing also supported efforts to produce personalized or patient-tumor-specific treatments, but finding a clear correlation between sequence profiles and therapeutic efficacy remains elusive. Patients with TNBC typically receive chemotherapy; however, recurrence rate remains high and the development of chemotherapy resistance occurs frequently. And finally, dissemination of TNBC is a major clinical issue, particularly considering that the predominant lung, brain,

<sup>1</sup>Oncofactory SAS, 8 Avenue Rockefeller, 69008 Lyon, France

<sup>2</sup>Erytech Pharma, Research and Development Department, 60 Avenue Rockefeller, 69008 Lyon, France

<sup>3</sup>Institut NeuroMyoGène, University of Lyon, University of Lyon 1 Claude Bernard Lyon 1, NeuroMyoGene Institute, CNRS UMR5310, INSERM U1217, 69007 Lyon, France

<sup>4</sup>Translational Research Department, Institut Curie, 26 Rue d'Ulm, 75005 Paris, France

<sup>5</sup>These authors contributed equally

<sup>6</sup>Senior authors

<sup>7</sup>Lead contact

\*Correspondence: celine.delloye@univ-lyon1.fr (C.D.-B.), valerie.castellani@univ-lyon1.fr (V.C.)

<https://doi.org/10.1016/j.isci.2021.103423>



and bone metastases remain incurable (Medina et al., 2020; Vagia et al., 2020). Accordingly, the development of novel therapeutic options for TNBC continues to be a high priority.

A variety of murine models, based either on engraftment of breast cancer cells or on genetically engineered tumorigenesis, have been developed to elucidate the mechanisms underlying tumor development, response to therapy, and acquired chemotherapeutic resistance (Park et al., 2018). Despite the utility of these models, comprehensive studies modeling patient tumor heterogeneity for biomarker discovery are lacking. To address this unmet need, grafting of tumor cells onto the chorioallantoic membrane of the avian egg has been considered as an alternative of murine xenografts. However, despite the advantages of such a simple *in vivo* model, tumor growth varies substantially in the extra-embryonic environment, in stark contrast to the growth observed in the context of a tumor-infiltrated organ.

Seeking to overcome the foregoing limitations, we recently reported on the successful modeling of pediatric neuroblastoma in the avian embryo (Delloye-Bourgeois et al., 2017). To more accurately mimic the *in vivo* milieu, we grafted neuroblastoma cells within tissues expected to provide a microenvironment representative of their cellular origin. This strategy proved highly effective in recapitulating key aspects of the disease, revealing that the embryonic environment provides a relevant context in which to model tumor growth and dissemination. Indeed, mechanisms at work during development and tumorigenesis have emerged over years as being closely related. For example, numerous studies have reported physiopathological conditions in which cancer cells take advantage of signaling pathways such as Wnt, sonic hedgehog (SHH), TGF, or BMP, acknowledged for their key contributions to embryonic development (Wakefield and Hill, 2013).

In breast cancer, this phenomenon manifests itself in the form of molecular communication between tumor cells and bone stroma that lie at the core of metastasis progression (Sethi and Kang, 2011). The bone microenvironment consists of mineralized extracellular matrix and various resident cell types, including osteoblasts, osteoclasts, mesenchymal stem cells, bone marrow endothelial cells, hematopoietic cells, and adipocytes. Bone homeostasis relies on the coordinated activity of osteoclasts and osteoblasts resorbing and renewing bone matrix, respectively. Such renewal processes are analogous to bone formation in the developing embryo, and perhaps unsurprisingly, involve developmental signaling pathways as attested by multiple studies (Mukherjee et al., 2018; Sethi and Kang, 2011; Wakefield and Hill, 2013; Ye and Jiang, 2016). For example, CXCR4/CXCL12 signaling plays a prominent role in several processes during embryogenesis, as demonstrated by the phenotypes resulting from ligand and receptor gene deletions (Kawaguchi et al., 2019; Nagasawa et al., 1996), and also controls key processes of bone physiology in adults (Kawaguchi et al., 2019). Interestingly, cancer cells establishing metastases in bone participate in these molecular exchanges, exploiting secreted signals normally reserved for osteoblasts and hematopoietic stem cells (Hiraga, 2019). Likewise, it has been recently established that upregulated CXCR4 expression enables some cancer cells to metastasize to bone (Coniglio, 2018; Hiraga, 2019). Once there, CXCR4 exerts a pro-osteolytic effect.

These parallels between embryonic development, homeostasis, and tumorigenesis led us to hypothesize that engrafting patient-derived tumor cells in embryonic regions committed to form tumor-relevant tissues would yield a microenvironment supportive of tumor formation. In this study, we report the creation of an *in vivo* model encompassing the generation and analysis of miniaturized replicas of patient tumors in targeted regions of the chicken embryo and their evaluation in preclinical studies. Breast cancer cells were implanted into a selected embryonic region, which was committed to form bones, to mimic a prominent metastatic site of breast cancer. We show using both the MDA-MB-436 TNBC cell line and patient biopsies that our avian model is remarkably effective in promoting rapid tumor intake (e.g., about 24 h), even when the initial number of cells is small. We also report the establishment of intravenous administration of standard therapies and the analysis of their efficacy on a series of patient tumor replicas. We further demonstrate that our patient tumor replicas allow for the coordinated evaluation of therapy-induced changes in both tumor genotype and phenotype. Finally, the exploitation of our innovative model for preclinical investigations was validated using L-asparaginase (ASNase), an active substance of a therapy currently being evaluated in several clinical trials (e.g., Erytech's TRYbeCA-1 and TRYbeCA-2, evaluating the efficacy of red cell-encapsulated ASNase against pancreatic cancer and TNBC, respectively). Altogether, our study establishes the patient-derived xenograft avian model (AVI-PDX) as an innovative tumor model for preclinical programs, which opens new avenues for the evaluation of mono and combination therapies and the characterization of signatures predictive of patient responses.

## RESULTS

### Micrografting breast cancer cells in the developing somites of the avian embryo

To design a model of tumorigenesis mimicking bone metastasis, we thought to target particular somites of the developing avian embryo. Somites are transient bilateral epithelial structures, each having a spheroidal shape. They are generated within the paraxial mesoderm (also referred as the presomitic mesoderm) according to a metamer pattern along the rostro-caudal body axis of the embryo (Maschner et al., 2016). Somites provide the basis for the vertebral column and ribs, also giving rise to bone and trunk musculature derivatives (Williams et al., 2019). Over the years, the chick embryo has become a reference model and its extensive use has contributed significantly to major advances in our understanding of developmental biology in vertebrates. Accordingly, somitogenesis has been very well documented, including extensive reporting on spatial and temporal hallmarks, which allowed us to appropriately place patient-derived tumor cells during the grafting procedure (Berti et al., 2015; Pourquié, 2018).

Furthermore, chicks and humans have similar numbers of somites, whereas mice have about 10 additional pairs. Newly generated somites, staged I–II according to Christ and Ordahl, are epithelial spheres with a central cavity, the somitocoel, filled by mesenchymal cells. From stage III, the ventral mesenchymal compartment becomes distinct from the dermomyotome dorsal one, the latter expressing specific transcription factors including Pax3 and Pax7 (Berti et al., 2015; Pourquié, 2018). Ventral cells dissociate through epithelio-mesenchymal transition to form the sclerotome and begin to express specific regulator genes such as *pax1*, and thereafter *pax9*, under the influence of morphogens released by surrounding floor plate and notochord tissue organizers, as well as by the surface ectoderm and the neural tube. In the chicken embryo, the first somite pair is visible at stage 7 according to Hamburger and Hamilton staging (HH7, 23–26 h post-gestation) (Hamburger and Hamilton, 1992). During stage HH14 (50–53 h post-gestation), a stage that we had previously found convenient for grafting procedures (Delloye-Bourgeois et al., 2017), 22 somite pairs are formed. Also, around this time, somite compartmentalization has already occurred for the oldest somites, including ventral cells progressing toward sclerotome differentiation under the control of various signals. Interestingly, several molecular signals reported to promote the establishment of metastatic foci in the bones are expressed during somitogenesis. This holds true for the chemokine CXCL12/SDF-1, WNTs, and HGF, as well as extracellular matrix proteins such as tenascins and fibronectins (Cléardin et al., 2021; Graf et al., 2021; Kar et al., 2020; Previdi et al., 2010; Scaal et al., 1999; Stebler et al., 2004; Tomás et al., 2011).

We used a well-characterized TNBC cell line, MDA-MB-436, to determine whether this presumptive skeletal embryonic region could support survival and growth of breast cancer cells. Cells were labeled with the vital fluorochrome carboxyfluorescein succinimidyl ester (CFSE) and systematically grafted within somites 12 and 13 of multiple HH14 embryos. After 48 h, HH25 embryos were collected (Figure 1A). Systematic fluorescence detected with a stereomicroscope was indicative of the presence of MDA-MB-436 cells in 100% of grafted embryos (Figure 1B). We took advantage of confocal light sheet microscopy to establish a procedure for the analysis of tumor cells at the whole organism level. Embryos were fixed and subsequently cleared using the ethyl cinnamate procedure. Notably, we consistently observed the formation of tumor masses within the developing somites, with a few cells escaping from these dense masses (Figure 1B). Histological analysis of formed tumors confirmed the organization of grafted cells in cohesive masses (Figure S1A) and their localization affixed to the Pax7<sup>+</sup>-dermomyotome compartment of the developing somite (Figure S1B). We then set up an analytic pipeline to precisely measure the volume occupied by tumor cells (Figure 1B). Tumor sizes suggested that MDA-MB-436 cells proliferated within the somitic environment. We further performed a Ki67 immunolabeling on cryosections of the embryos, which confirmed a high mitotic index of grafted MDA-MB-436 cells, with a mean of 34% of Ki67<sup>+</sup> cells among analyzed cryosections (n = 10) (Figure 1C). Thus, our model induces TNBC cells to take root within the developing somitic environment, to proliferate, and to form measurable tumor masses with ubiquitous and reproducible tumor intake occurring in no more than 48 h.

### Administration of SOCs in the avian model recapitulates TNBC response to standard anticancer therapies

We next wanted to understand whether our tumor model would respond to current anticancer therapies similarly to how patient tumors respond *in vivo*, with the goal of creating a model relevant for preclinical studies. We chose to work with two major standards of care (SOCs), gemcitabine and carboplatin, commonly used in the treatment of TNBC.

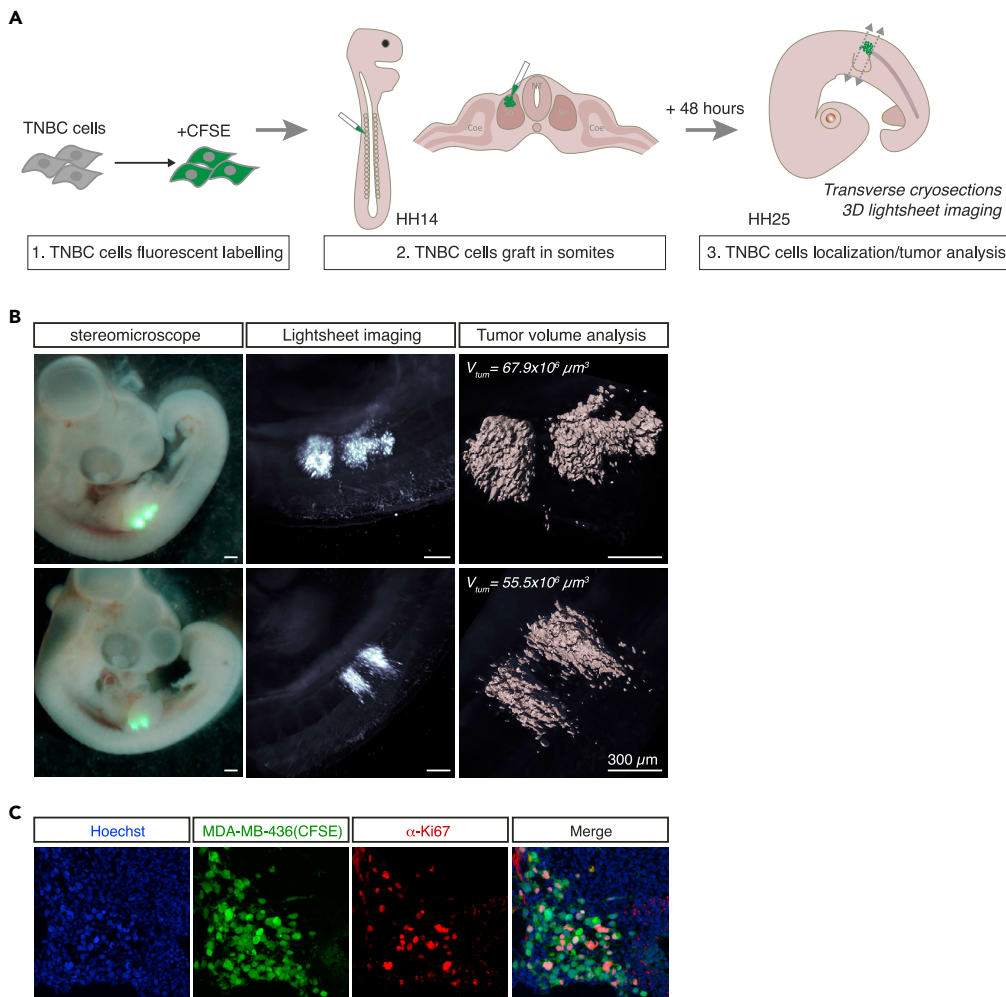


**Figure 1. Grafting of MDA-MB-436 TNBC cells within developing somites allows tumor formation and proliferation**

(A) Setup of TNBC cell grafting in the developing somites: TNBC cells are labeled with CFSE and microinjected in the developing somites at HH14 stage. Grafted embryos are harvested for imaging analysis 48 h after the graft, at HH25 stage.

(B) Detection and volumetric analysis of TNBC tumor masses formed 48 h after the graft: TNBC fluorescent masses are detected with a stereomicroscope (left panels) and next imaged in whole cleared embryos using lightsheet imaging (middle panels), which allows a precise quantification of tumor volumes using Imaris 3D software (right panels).

(C) Detection of Ki67+ proliferating cells by immunofluorescence (in red) on cryosections of MDA-MB-436 tumor masses (in green, CFSE+) formed in HH25 chick embryos. Chick and human nuclei are labeled with Hoechst (in blue). See also [Figure S1](#) for further histological and immunofluorescence characterizations. Scale bars, 300  $\mu\text{m}$ .

First, we set up a procedure to determine optimal doses of drugs. Having access to the vascular network of the chorioallantoic membrane that irrigates the developing embryo, we performed intravenous injections of increasing doses of gemcitabine or carboplatin, in multiple HH20 chick embryos (approximately 72 h post-gestation) ([Figure 2A](#)). To determine the maximum tolerated dose (MTD), we established a list of criteria that we examined 24 h post-injection (HH25 embryos) including survival of the embryo, morphological checkpoints, and global growth by measuring the Body Surface Area (BSA), as detailed in [STAR Methods](#) ([Figure 2A](#)). A survival rate below 75% was indicative of dose toxicity, excluding further examination of the concerned group. The correct stage-related development of embryos was systematically assessed by checking their craniofacial morphology (presence of each cerebral compartment and eyes), the presence of four limb buds, their cardiac morphology, and the anatomy of embryonic annexes such as the allantois. For gemcitabine, we observed that doses higher than 17.1 mg/kg induced massive

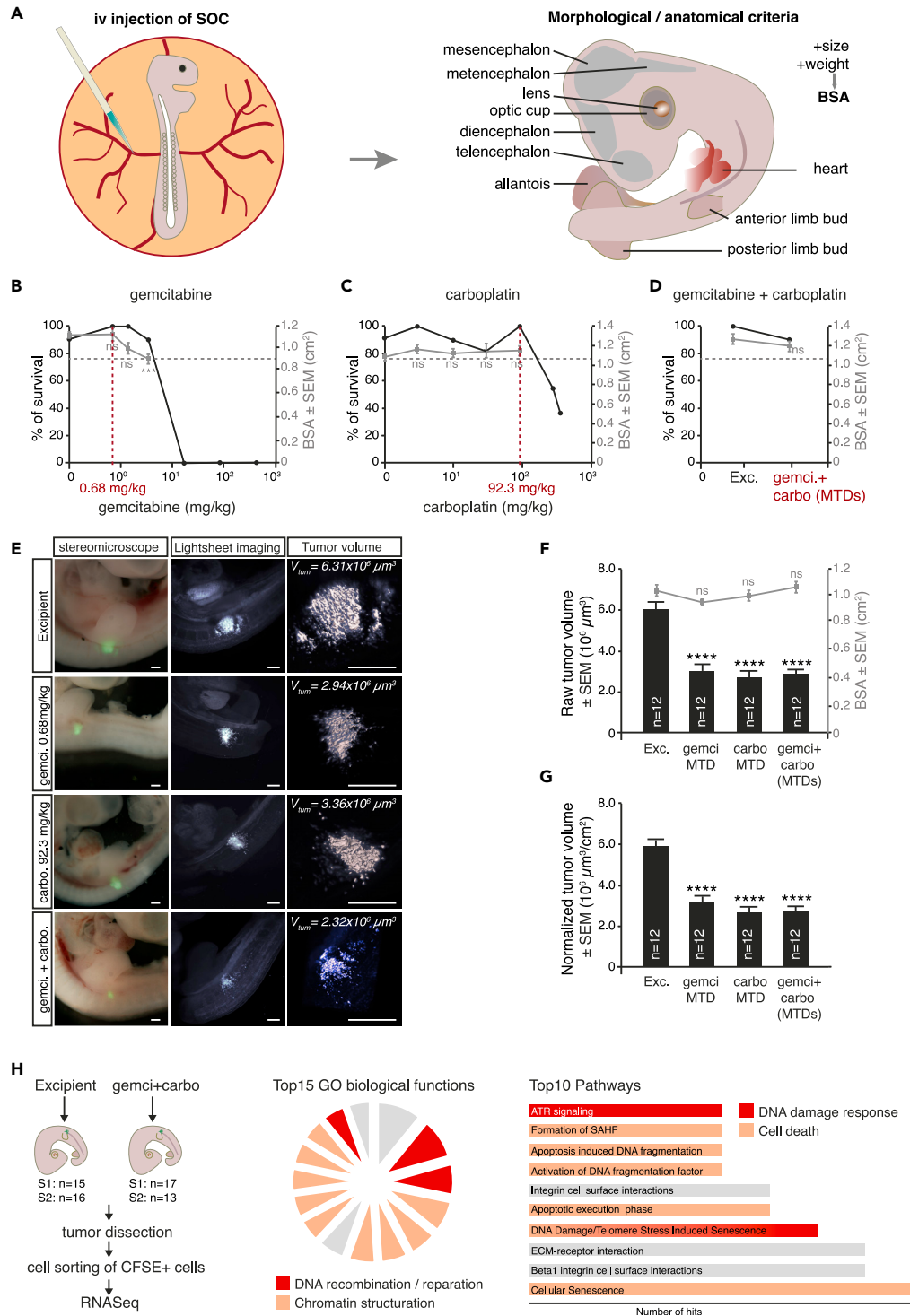


**Figure 2. Administration of SOCs in the avian model efficiently triggers anticancer response of grafted TNBC cells**

(A) Schematic representation of the procedure of intravenous SOC administration in the avian model (left panel) and illustration of morphologic, anatomical, and morphometric criteria analyzed for each embryo after drug administration (right panel).

(B–D) Survival rate (left axis) and mean body surface area (BSA, right axis) of chick embryos injected with increasing doses of gemcitabine (B), carboplatin (C), or combination of both maximum tolerated doses (MTDs) (D). Each dose was

**Figure 2. Continued**

administered to a minimum of 10 embryos, using excipient (NaCl) as a control. The MTD of gemcitabine and carboplatin was defined as the higher dose of drug associated with a survival rate higher than 80% and a mean BSA similar (i.e., non-statistically different) from embryos treated with NaCl. MTDs are indicated in red on the abscissa axis. Data are represented as mean  $\pm$  SEM. \*\*\* $p < 0.001$ ; ns, non-significant using Student's t test compared with excipient.

(E–G) Analysis of tumor growth by 3D lightsheet imaging and tumor volumetric analysis (E) of chick embryos treated with gemcitabine MTD ( $n = 12$ ), carboplatin MTD ( $n = 12$ ), a combination of both ( $n = 12$ ), or excipient ( $n = 12$ ) in a series of chick embryos grafted with MDA-MB-436 cells. Scale bars, 300  $\mu\text{m}$ . Mean raw tumor volumes and mean BSA for each experimental condition was measured (F). Mean tumor volumes normalized on mean BSA are also reported to take into account slight variability of embryonic growth (G). Error bars indicate SEM. \*\*\*\* $p < 0.0001$ . ns, non-significant using Student's t test compared with excipient. See also [Figure S2](#) for further characterization of SOCs' effect on grafted TNBC cells.

(H) Whole RNA-seq analysis of MDA-MB-436 cells sorted from series of grafted chick embryos treated either with excipient or with a combination of gemcitabine and carboplatin MTD. The procedure is illustrated in the left panel, and the number of embryos for each of the two replicates is indicated. Ninety-one differentially expressed transcripts ( $\text{padj} < 0.05$  and fold change  $> 1.5$ ) and 111 "ON/OFF" transcripts were considered for global analysis of biological functions (middle panel) and signaling pathways (right panel) concerned by gene expression change. Within the 15 most significantly regulated biological functions, the ones related to DNA recombination/repair and chromatin structuration are highlighted on the diagram. Pathways related to DNA damage response and/or cell death are highlighted within the top 10 significantly regulated pathways.

embryonic death. Doses between 1.37 and 3.42 mg/kg were associated with a survival rate above 75%, but significantly affected global growth (as measured by the BSA criteria) and morphological checkpoints. We thus fixed the gemcitabine MTD at 0.68 mg/kg in chick embryos ([Figure 2B](#)). Following the same procedure, the carboplatin MTD was determined to be 92.3 mg/kg ([Figure 2C](#)). As gemcitabine and carboplatin are frequently used as a combi-therapy, simultaneous injection of gemcitabine and carboplatin MTDs was tested in multiple HH20 chick embryos ([Figure 2D](#)). We could observe that the co-treatment was perfectly tolerated *in ovo*, according to the criteria listed in this section.

We next assessed whether administration of gemcitabine and carboplatin MTDs, alone or in combination, could impact on MDA-MB-436 tumor growth in the avian embryo. TNBC cell line was described to be sensitive to both SOCs in a range of *in vitro* and *in vivo* studies ([Larsson et al., 2020](#); [Mintz et al., 2020](#)). Each SOC MTD was injected intravenously in randomized batches of avian embryos 24 h after engraftment of MDA-MB-436 cells. After 24 h of SOC administration, embryos were harvested and tumor volumes were analyzed by light sheet microscopy and subsequent 3D image analysis, as described in [Figure 1](#) ([Figure 2E](#)). Administration of gemcitabine and carboplatin alone or in combination induced a significant decrease in mean tumor volume, without affecting the global embryonic growth ([Figures 2F](#) and [2G](#)). Each SOC alone drastically affected tumor growth, whereas the simultaneous administration of both did not trigger any additive effect on MDA-MB-436 tumors when compared with single SOC administrations. To investigate the mode of action of gemcitabine and carboplatin in grafted TNBC cells, we first quantified the mitotic index on cryosections of chick embryos 24 h after injection of SOCs. We noted a decrease in the number of phospho-Histone H3 (PHH3)-positive cancer cells upon SOCs treatment compared with control ([Figure S2A](#)). Furthermore, the antitumor activity of gemcitabine and carboplatin has been shown to induce an increase in the DNA damage marker phospho- $\gamma\text{H2AX}$  in several types of cancer ([Ewald et al., 2007](#); [Jin et al., 2013](#)). We observed a significant increase in the number of MDA-MB-436 cells expressing phospho- $\gamma\text{H2AX}$  following SOCs treatment compared with control ([Figure S2B](#)). These data highlight the genotoxic activity of gemcitabine and carboplatin interfering with the growth of TNBC cells in our avian model. Thus, within a brief window of time, 24 h, our avian model of breast cancer cell grafting within the developing somites of chick embryos recapitulates tumor growth and tumor response to SOCs.

**RNA-seq analysis of gemcitabine/carboplatin-triggered transcriptional regulations in tumors formed in the avian embryo**

Next, we asked whether we could combine our *in vivo* tumor model with large-scale analyses to evaluate the impact of SOCs on TNBC cells at the molecular level. We micro-dissected the tumors from a series of grafted embryos and treated them with either the excipient or with a combination of gemcitabine and carboplatin. For each condition, tumor cells embedded in the chick embryonic tissues were dissociated and sorted for bulk RNA sequencing (RNA-seq) ([Figure 2H](#)). Given the small number of replicates (duplicates for each condition), we chose to select stringent parameters to perform the differential expression analysis, to

avoid false-positive findings, as described in the [STAR Methods](#). Using these criteria, the analysis revealed a set of 91 transcripts significantly regulated in chemo-treated tumors when compared with excipient ( $p_{adj} < 0.05$ , fold-change  $> 1.5$ ) and 111 transcripts whose expression was detected only in one of the two experimental conditions ("ON/OFF" transcripts, as explained in the [STAR Methods](#)). This list of 202 transcripts was further investigated with ToppGene software (<https://toppgene.cchmc.org>) to assign key biological functions and signaling pathways impacted by gemcitabine/carboplatin treatment. Notably, among the 15 top biological functions represented, 12 were related to DNA repair/recombination processes and to the regulation of chromatin structure ([Figure 2H](#)). Similarly, among the top 10 signaling pathways associated with gene expression regulation upon gemcitabine/carboplatin treatment, 7 were directly related to DNA damage response, apoptosis, and senescence induction ([Figure 2H](#)). Interestingly, these findings are in accordance with well-described modes of action of gemcitabine and carboplatin in the clinic, which include the targeting of DNA replication and repair mechanisms, leading to the activation of DNA damage response and the subsequent death of chemosensitive cells.

### Adaptation of the micrografting technique to breast cancer patient samples: Creation of an avian patient-derived xenograft (AVI-PDX) model

To further extend our model, we next thought to test whether such a micrografting technique could be adapted to fresh or frozen patient samples, without any intermediate culture step potentially altering the tumoral features. We selected 15 different patient samples with diverse origins and preparation modalities: "rough" patient samples without any experimental handling ( $n = 11$ ); patient samples derived from murine PDX models ( $n = 4$ ); fresh ( $n = 6$ ) and DMSO-cryopreserved ( $n = 9$ ) samples; and samples originating from primary tumors ( $n = 10$ ) or brain metastases ( $n = 5$ ) ([Figure 3A](#)). Each sample was dissociated and the global cell content was labeled with CFSE before engraftment. The tumor establishment rate 48 h after the implantation was remarkably above 70% for all samples tested except for OF-BRE-007 for which it was 34%. Tumor size 48 h after engraftment was homogeneous among embryos engrafted with the same sample cell content, whereas the mean tumor volume for each sample varied between  $7.13 \times 10^3$  and  $2,830 \times 10^3 \mu\text{m}^3$ , indicating heterogeneity in tumor sample cell content and/or behavior within avian embryonic tissues ([Figures 3A and 3B](#)). Thus, we were able to generate 14 avian PDX (AVI-PDX) models from breast cancer patient samples, with homogeneous tumor growth among embryonic replicates and with an exceptionally fast and high rate of tumor intake. We tested the effect of gemcitabine in combination with carboplatin in 4 AVI-PDX models obtained from 4 rough TNBC patient samples, 2 primary tumors and 2 brain metastases ([Figure 3C](#)). Comparison of tumor volumes between excipient and SOC-treated embryos revealed that the two AVI-PDX models (OF-BRE-002 and OF-BRE-nbt311) did show a significant anticancer response to SOC, whereas the two others (OF-BRE-012 and OF-BRE-nbt783-derived AVI-PDX) were completely resistant to SOC administration. Thus, tumor replicas from different patients exhibited response heterogeneity, which is a hallmark of actual TNBC patient tumors in the clinic.

### Preclinical evaluation of L-asparaginase efficacy in TNBC treatment using the AVI-PDX system

These results indicated that the AVI-PDX model might be highly relevant and valuable for evaluating the efficacy of candidate therapeutic compounds. ASNase hydrolyzes L-asparagine (ASN) and glutamine (GLN) into aspartic and glutamic acids and ammonia, leading to ASN and GLN removal from the circulation, which in turn causes metabolic dysfunction, cell-cycle arrest, apoptosis, and tumor starvation. ASNase is routinely used in the treatment of some hematological malignancies, most notably acute lymphoblastic leukemia ([Ahlke et al., 1997](#); [Estlin et al., 2000](#); [Müller and Boos, 1998](#)).

To assess the impact of ASNase on tumor cell survival *in vitro*, we first conducted experiments with the MDA-MB-436 TNBC cell line ([Figure 4A](#)). The objective was to evaluate the *in vitro* sensitivity of this cell line to recombinant *E. coli* ASNase alone by determination of the concentration of drug that gives a 50% inhibition of cell viability (IC50). Although cytotoxicity curve profiles showed some heterogeneity, the IC50 determination remained reproducible between experiments. On day 4, a dose-response and a similar plateau effect were observed for doses of ASNase from 1 to 10 U/mL. However, 10% of cells still remained viable at even the highest concentration tested (10 U/mL). The mean IC50 of ASNase from the 3 experiments on MDA-MB-436 cells after a 4-day exposure was determined to be  $0.19 \pm 0.06$  U/mL.

Next, we measured ASNase tolerance in the avian embryo to estimate its maximum tolerated dose ([Figure 4B](#)). Intravenous injection of increasing doses of ASNase (150 U/kg to  $1.22 \times 10^5$  U/kg) in E3 chick

**A**

	Sample ID	Origin	Classification	Nb of grafted embryo	Tumor intake rate	Mean tumor volume $\pm$ SEM ( $10^3 \mu\text{m}^3$ ) w/o treatment
Patient samples	OF-BRE-001	Primary tumor surgery (fresh)	TNBC; invasive ductal carcinoma	26	69%	3.06 $\pm$ 0.653
	OF-BRE-nbt219	cerebral metastasis (frozen)	TNBC; invasive ductal carcinoma	41	100%	2830 $\pm$ 430
	OF-BRE-nbt1111	cerebral metastasis (frozen)	TNBC; invasive ductal carcinoma	23	100%	132.5 $\pm$ 13.5
	OF-BRE-nbt311	cerebral metastasis (frozen)	ER-, PR-, HER2int; invasive ductal carcinoma	73	97%	2670 $\pm$ 352
	OF-BRE-002	Primary tumor surgery (fresh)	TNBC	26	100%	20.6 $\pm$ 12.5
	OF-BRE-nbt783	cerebral metastasis (frozen)	TNBC; invasive ductal carcinoma	53	100%	721 $\pm$ 26.5
	OF-BRE-nbt494	cerebral metastasis (frozen)	TNBC; invasive ductal carcinoma	31	100%	1043 $\pm$ 212
	OF-BRE-007	Primary tumor surgery (fresh)	TNBC	47	34%	8.05 $\pm$ 3.23
	OF-BRE-012	Primary tumor surgery (fresh)	TNBC; invasive ductal carcinoma	34	94%	8.42 $\pm$ 1.45
	OF-BRE-016	Primary tumor surgery (fresh)	TNBC; invasive ductal carcinoma	27	89%	7.13 $\pm$ 3.17
	OF-BRE-017	Primary tumor surgery (fresh)	TNBC	91	91%	55.9 $\pm$ 2.52
Murine PDX	OD-BRE-0503	Primary tumor surgery (frozen)	TNBC; invasive ductal carcinoma	19	100%	1020 $\pm$ 280
	OD-BRE-0589	Primary tumor surgery (frozen)	TNBC; carcinoma with metaplasia	19	100%	400 $\pm$ 70
	OD-BRE-0631	Primary tumor surgery (frozen)	TNBC; invasive ductal carcinoma	20	100%	830 $\pm$ 250
	OD-BRE-0733	Primary tumor surgery (frozen)	TNBC; invasive ductal carcinoma	21	100%	630 $\pm$ 110

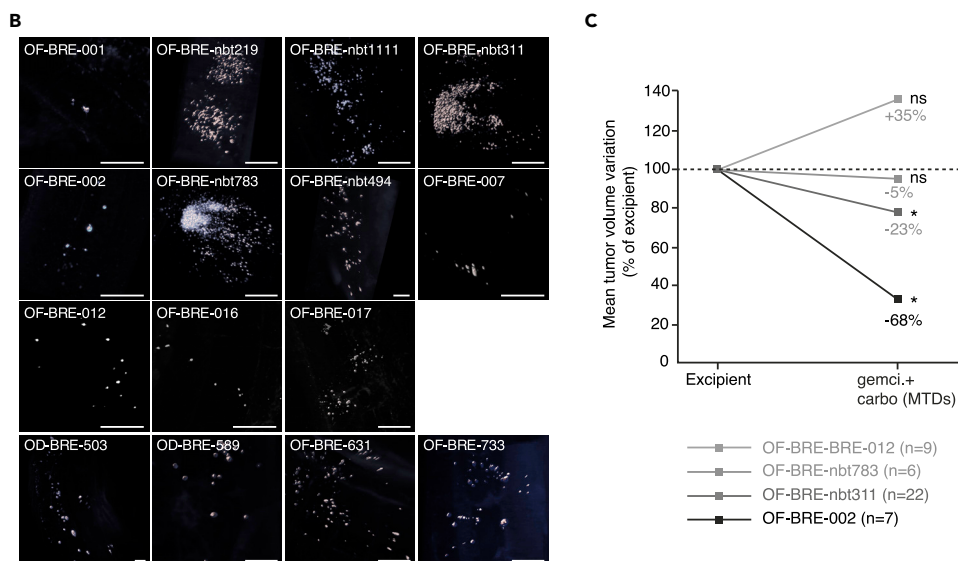


**Figure 3. The avian model is adapted to the micrograft of patient samples**

(A) Table recapitulating breast cancer sample characteristics—origin, classification—their behavior in the avian approach—tumor intake rate, mean tumor volume as measured by 3D lightsheet imaging, and subsequent volume measurement.

(B) Representative 3D lightsheet images obtained with each patient sample referenced in the (A). Scale bars, 300  $\mu\text{m}$ .

(C) Effect of gemcitabine/carboplatin administration in a series of embryos engrafted with 4 different patient samples, when compared with excipient administration. Tumor volumes were measured using lightsheet microscopy and 3D image analysis; results are presented as mean tumor volume variation in gemcitabine/carboplatin-treated embryos when compared with excipient-treated embryos. The number of embryos analyzed for each patient sample is indicated on the graph. \* $p < 0.05$ ; ns, non-significant using Mann-Whitney test compared with excipient.

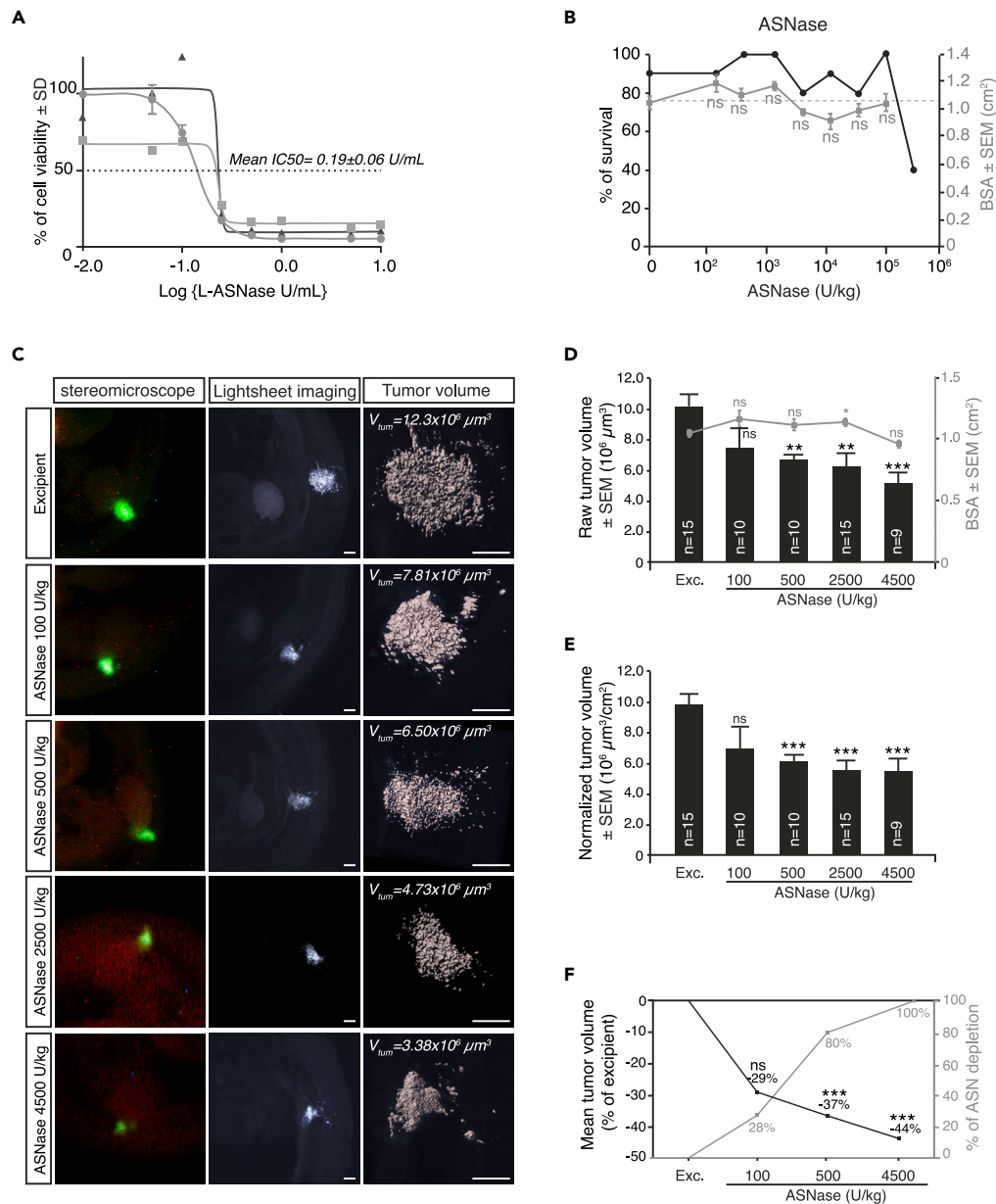


**Figure 4. Preclinical evaluation of L-asparaginase efficacy in TNBC using the avian model**

(A) *In vitro* evaluation of MDA-MB-436 cell viability, after treatment with increasing doses of ASNase. Three experimental replicates are presented, allowing to estimate a mean IC<sub>50</sub> of  $0.19 \pm 0.06$  U/mL. Data are presented as mean  $\pm$  SD.

(B) Survival rate (left axis) and mean body surface area (BSA, right axis) of chick embryos injected with increasing doses of ASNase. Each dose was administered to a minimum of 10 embryos, using excipient (NaCl) as a control. Error bars indicate SEM. ns, non-significant using Mann-Whitney test compared with excipient.

(C–E) Analysis of tumor growth by 3D lightsheet imaging and tumor volumetric analysis (C) of chick embryos 24 h after treatment with increasing doses of ASNase or excipient in series of chick embryos grafted with MDA-MB-436 cells. The number of embryos analyzed for each experimental condition is indicated on the graph. Scale bars, 300  $\mu$ m. Mean raw tumor volumes and mean BSA for each experimental condition was measured (D). Mean tumor volumes normalized on mean BSA are also reported to take into account slight variability of embryonic growth (E). Error bars indicate SEM. \*\* $p < 0.01$ ; \*\*\* $p < 0.001$ . ns, non-significant using Student's t test compared with excipient.

(F) Quantification of plasma ASN in a series of chick embryos 24 h after intravenous injection of increasing doses of ASNase when compared with excipient, to estimate ASN reduction rate. A minimum of 10 embryos per condition were used to harvest blood samples. Reduction rates are presented together with the corresponding mean tumor volume variations when compared with control, obtained in the avian model grafted with MDA-MB-436 cells.

embryos did not affect embryonic survival, morphogenesis, or global growth rate, reported by the body size area (BSA). At doses of  $3.57 \times 10^5$  U/kg and higher, embryo survival was compromised and largely fell below the 75% cutoff, indicating toxicity. Interestingly, 4,500 U/kg corresponds to a high dose in the avian embryo model and is quite below the total dose currently given in the clinic in repeated administration (superior to 10,000 U/kg). We thus chose to fix 4,500 U/kg as the maximum dose for further preclinical evaluation of ASNase efficacy.

We then evaluated the antitumor efficacy of increasing doses of ASNase, ranging from 100 to 4,500 U/kg, in a series of chick embryos engrafted with MDA-MB-436 cells. As set up for SOCs, a single administration of ASNase was performed 24 h after the graft, and treated embryos were harvested 24 h later for tumor growth analysis (Figures 4C–4E). The lowest dose (100 U/kg) did not affect tumor volume (neither raw nor embryonic growth rate-normalized volume), whereas higher doses each triggered a significant decrease in mean tumor volume without affecting global embryonic growth. Notably, in the MDA-MB-436 avian model, a slight dose effect of ASNase was observed with a mean decrease in raw tumor volume, increasing from 34% at 500 U/kg to 49% at 4,500 U/kg, and from 37% to 44% when the tumor volumes were normalized to embryonic growth. As ASNase acts by depleting cells of available ASN, we thought to examine whether these efficacy experiments correlated with plasma ASN levels in treated embryos. Blood was harvested from a series of embryos that received the different doses, for evaluation of plasma amino acid levels by high-performance liquid chromatography (Figure 4F). We confirmed that increasing doses of ASNase administrated intravenously triggered a dose-dependent reduction of plasma ASN, ranging from 28% of excipient at 100 U/kg to complete reduction at 4,500 U/kg. At 500 U/kg, ASN was depleted by 80%. These reduction rates mirrored the antitumor efficacy of ASNase, which was insignificant at 100 U/kg and increased from 500 to 4500 U/kg (Figures 4C–4E). Thus, ASNase enzymatic activity is effective and quantifiable in the avian embryo system, and its activity impedes MDA-MB-436 tumor growth in a dose-dependent fashion.

These first results encouraged us to further evaluate ASNase in AVI-PDX models, with the aim to set this candidate therapy against TNBC patient heterogeneity (Figure 5A). We worked with 500 and 4,500 U/kg doses of ASNase that were previously shown to trigger both satisfactory ASN and MDA-MB-436 tumor volume reductions in the avian embryo. Fourteen AVI-PDX models were engineered, among which nine showed an anti-tumor response to ASNase with at least one of the two doses tested (green samples in Figure 5A). Four of these AVI-PDX models were achieved on limited number of embryos, excluding the possibility of performing statistical analysis. Thus, we focused on the remaining 10 models, and our statistical evaluation confirmed that 60% of AVI-PDX responded significantly to ASNase treatment, irrespective of the origin of the patient sample (Figures 5B–5E).

### **Implementation of breast cancer micrografting technique in the avian embryo: Targeting the developing brain to model cerebral metastasis**

Last, we investigated whether we could develop an avian tumor model recapitulating another metastatic microenvironment relevant to TNBC pathology.

Metastasis to the brain is one of the hallmarks of aggressive breast cancer that appreciably affects disease outcome (Karginova et al., 2015). The brain microenvironment promotes the adaptation of highly specialized cancer cells and the formation of tumors possessing unique characteristics. Moreover, the ability of therapeutics to penetrate the blood-brain barrier continues to present a daunting challenge. Therefore, having a PDX model that could efficiently and robustly reproduce brain metastases would provide a complementary and powerful tool for the preclinical evaluation of candidate therapeutics. We engrafted either TNBC cells (MDA-MB-436) or 1 of 7 patient samples obtained from murine PDX, directly in the brain parenchymas of a series of HH14 chick embryos (Figure 6A). The MDA-MB-436 cell line grafted efficiently, leading to a very high rate of tumor intake rate (93%) 48 h after engraftment. Analysis of grafted embryos by confocal lightsheet microscopy confirmed the formation of tumor masses within the brain parenchyma of all embryos (Figures 6B and 6C). Moreover, a Ki67 immunolabeling performed on cryosections of grafted embryos revealed a high mitotic index of grafted MDA-MB-436 cells, with a mean of 41% ( $\pm 6.4\%$ ) of Ki67<sup>+</sup> cells (n = 4 fields) (Figure 6D). These data confirmed that TNBC cells are able to form tumors within the developing chick brain tissue and to continue proliferating. Patient samples obtained from 7 murine PDX (5 triple negative, 1 ER<sup>+</sup>, and 1 HER2<sup>+</sup>) were implanted in the brain parenchyma following the same procedure as for the 436 cells. The tumor intake rate was greater than 88% for each sample, establishing

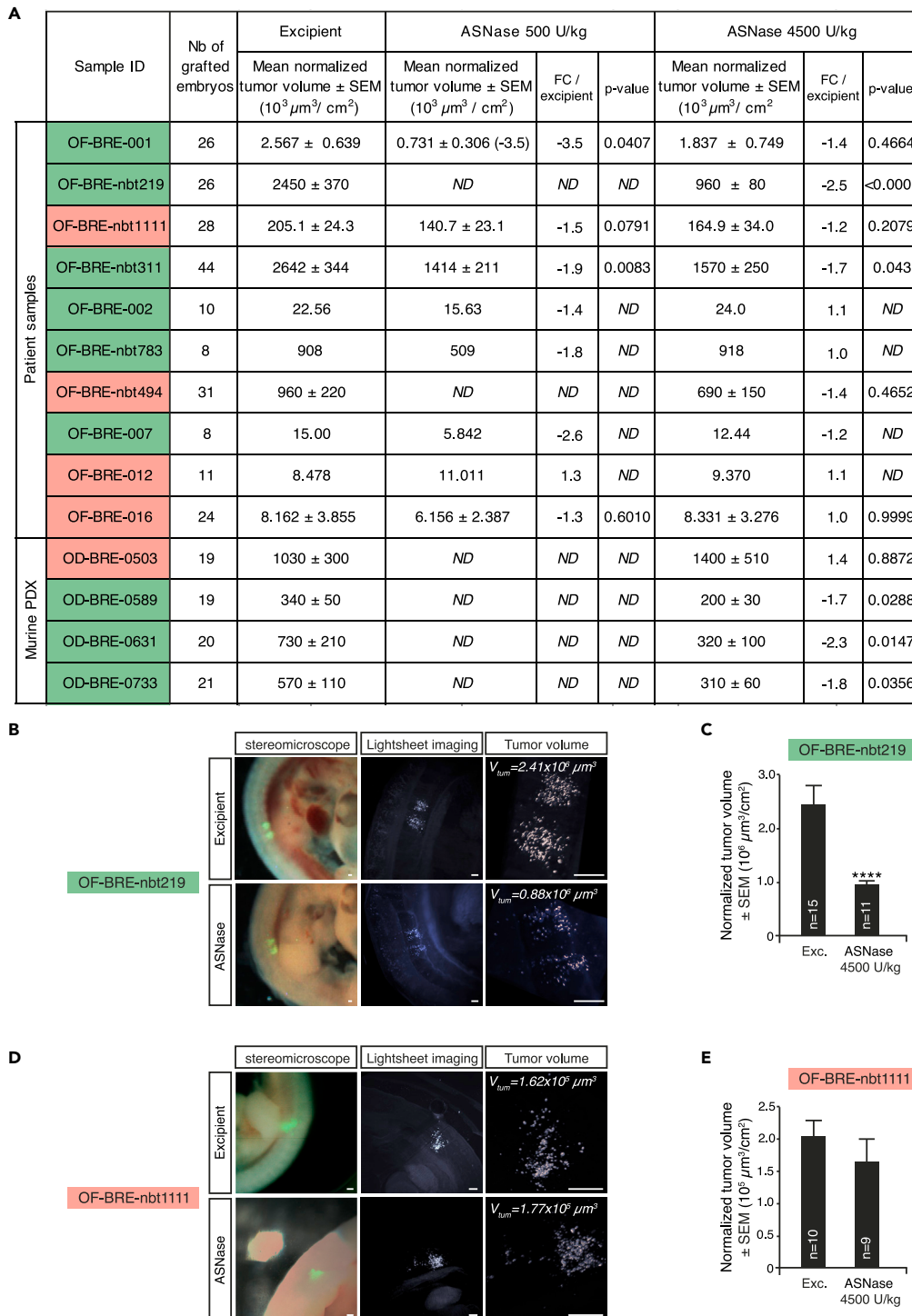


**Figure 5. Preclinical evaluation of L-asparaginase efficacy in the TNBC AVI-PDX model**

(A) Table recapitulating the effect of ASNase administration (500 and/or 4500 U/kg) on mean tumor volume (when compared with excipient) for each of the 14 patient samples grafted in the AVI-PDX system. Patient samples showing an anti-tumor response to ASNase are highlighted in green (9 of 14 samples), whereas non-responder patient samples are highlighted in red (5 of 14 samples). ND, not determined.

(B–E) Analysis of tumor growth by 3D lightsheet imaging and tumor volumetric analysis (B and D) of chick embryos 24 h after treatment with increasing doses of ASNase or excipient in series of chick embryos grafted with OF-BRE-nbt219

**Figure 5. Continued**

(responder [B and C]) or OF-BRE-nbt1111 (non-responder [D and E]) TNBC samples. Scale bars, 300  $\mu\text{m}$ . Mean tumor volumes normalized on mean BSA are reported for each patient sample in excipient- and ASNase-treated series of embryos (C and E). The number of embryos analyzed for each experimental condition is indicated on the graph. Error bars indicate SEM. ns, non-significant, \*\*\*\*p < 0.0001, using Mann-Whitney test.

the developing brain parenchyma as an environment of choice for breast tumor cell survival and growth (Figures 6A and 6E). Furthermore, depending on the patient sample, we noted different tumorigenic behaviors, ranging from dense, localized tumor masses to numerous small tumor foci implanted in the parenchyma or floating in the cerebrospinal fluid (Figure 6E). Thus, we succeeded with our *in vivo* model to establish various metastatic models that allow tumor cells to be subjected to different microenvironments and therapeutic regimens.

**DISCUSSION**

Our study introduces an innovative *in vivo* paradigm to model breast cancer tumorigenesis and applications of this model to various preclinical investigations. When implanted in targeted tissues of the avian embryo, human TNBC cells from diverse origins such as cell lines, murine PDX, patient biopsies, and resections (from both primary and metastatic foci) were all fully capable of surviving and forming tumors in a rapid and reproducible manner. As we expected, the somitic region committed to becoming skeletal tissues provides a favorable microenvironment to TNBC cells. Notably, none of the 11 engrafted patient samples resulted in failure of tumor intake, with a greater than 90% success rate for 8 of them. This makes our innovative model ideally suited for statistical analysis of tumor volumes and quantitative comparison of experimental conditions. Administration of therapeutic compounds into grafted embryos and subsequent 3D analysis of tumor volumes revealed that with our process, drug effects can be detected in as little as 1 day post-treatment, which opens new avenues for rapid screening therapeutic strategies. We also demonstrated that our *in vivo* model is adapted to the sorting of miniature tumors, and the running of large-scale molecular analysis on sorted tumor cells, which thus enable deep characterization of the mechanisms of action of therapeutic compounds.

Our avian model of tumor cell transplantation offers an alternative to mouse xenograft models, often associated with low and heterogeneous tumor intake, difficulties to mimic metastatic extension, high cost, and strong ethical pressure. In regard to these limitations, the avian PDX model value includes, among others, a strong predictive power, a high reproducibility coupled with tumor intake efficiency and the possibility to perform robust statistics, a miniaturized scale of experimentation that fits with the size of patient biopsies, and the use of a species in accordance with ethical guidelines. Our results also suggest that particular phenotypical features, associated with tumor properties, could be revealed upon engraftment in the embryonic tissues. The somitic microenvironment does not fully recapitulate that to which metastatic cancer cells are exposed in the bone, in particular because it lacks immune cells and blood vessels. Nevertheless, although immature, this somitic territory holds interesting molecular similarities with the bone tissue. Likewise, signaling reported for their instructive role during the bone metastatic process like CXCL12/SDF-1, WNT, and HGF, as well as extracellular matrix components like tenascin-C or fibronectins, are also present in the developing somitic domain (Clézardin et al., 2021; Graf et al., 2021; Kar et al., 2020; Previdi et al., 2010; Scaal et al., 1999; Stebler et al., 2004; Tomás et al., 2011). This likely contributes to define the behaviors of grafted tumoral cells.

Our results with gemcitabine and carboplatin (SOCs for patients with TNBC) are consistent with those reported with murine models and in the clinic (Karginova et al., 2015; Maisano et al., 2011; Ou et al., 2020).

First, we could reproduce the responsiveness of MDA-MB-436 cells to gemcitabine and carboplatin (Karginova et al., 2015; Sasaki et al., 2014).

Second, our transcriptomic analysis comparing tumors formed in the avian tissues that were exposed to the gemcitabine/carboplatin combination and excipient revealed a landscape of gene pathway regulation that is fully consistent with the mode of action of these chemotherapies. Similar to other platinum derivatives, carboplatin covalently binds to the N7 site of purine bases, interfering with cell replication, which drives the cells toward apoptosis or necrosis (Schoch et al., 2020). Gemcitabine is an analog of deoxycytidine and its active, phosphorylated form interferes with DNA synthesis (Plunkett et al., 1995). Among the top gene pathways identified, most were related to DNA damage response and cell death. These findings demonstrate that 24-h exposure of engrafted tumor cells to these chemotherapies through delivery via the general circulation reproduces their

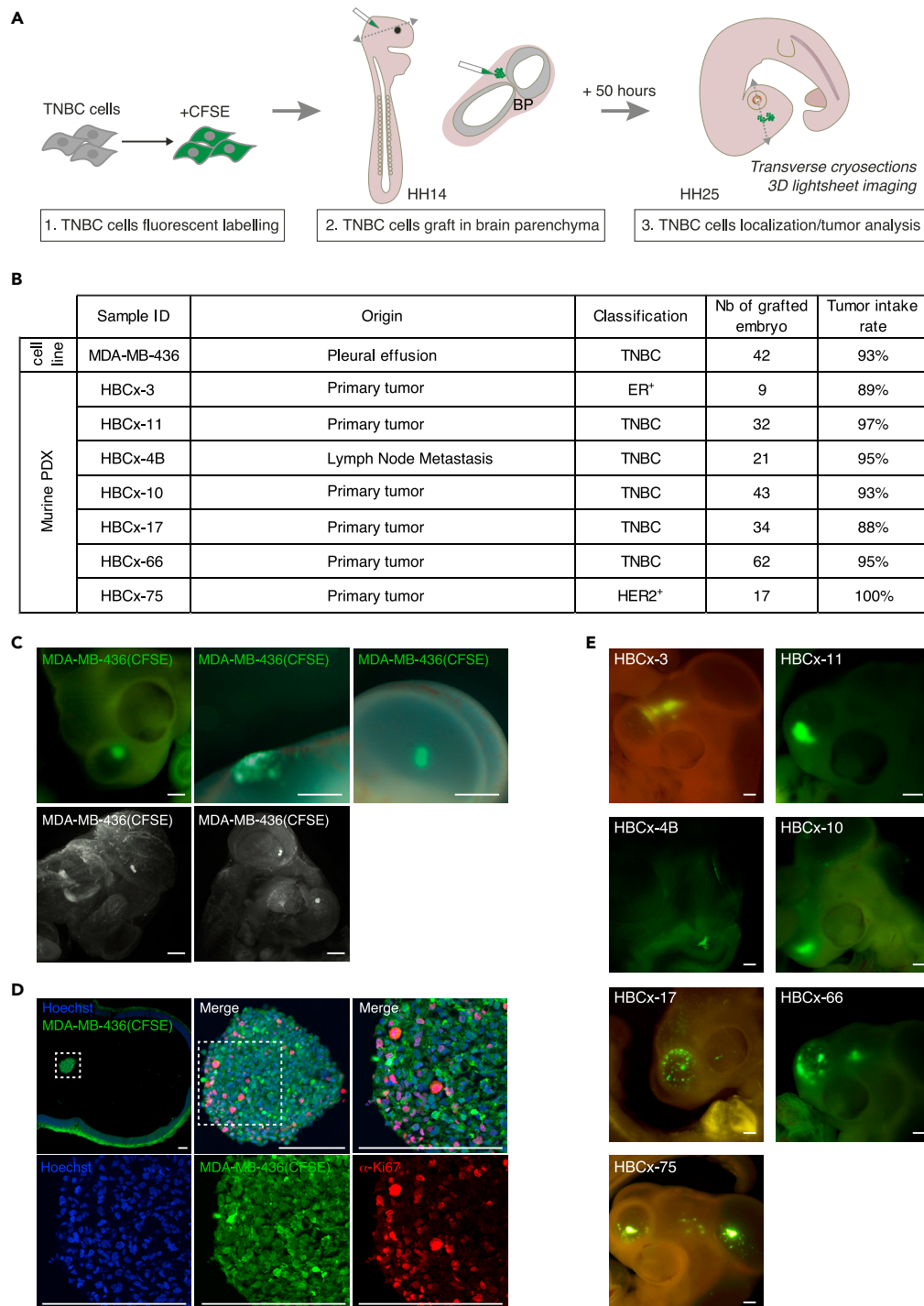


**Figure 6. Targeting the developing brain to model TNBC cerebral metastasis in the avian embryo**

(A) Setup of TNBC cells grafting procedure in the developing brain parenchyma (BP): TNBC cells are labeled with CFSE and microinjected in the developing BP at HH14 stage. Grafted embryos are harvested for imaging analysis 48 h after the graft, at HH25 stage.

(B) Table recapitulating breast cancer samples characteristics—origin, classification—and their corresponding tumor intake rate in the avian BP.

(C) Representative images of classical localization of MDA-MB-436 cells in the developing head 48 h after the graft as observed with the stereomicroscope (upper panels) or by 3D lightsheet imaging (lower panels). Scale bar, 300  $\mu$ m.

**Figure 6. Continued**

(D) Detection of Ki67+ proliferating cells by immunofluorescence (in red) on cryosections of MDA-MB-436 tumor masses (in green, CFSE+) formed in the developing brain of chick embryos. Chick and human nuclei are labeled with Hoechst (in blue). Scale bars, 100  $\mu$ m.

(E) Representative images of breast cancer patient cells in the developing head 48 h after the graft as observed with the stereomicroscope. Scale bars, 300  $\mu$ m.

expected outcome. This demonstrates the strength of both our *in vivo* model and its companion procedure for RNA-seq analysis of chemotherapy-treated tumors grown in the avian embryo.

Third and interestingly, when the avian model was applied to 4 patient samples, we observed a significant reduction in avian tumor replica volume following SOC administration for half of them, with one case showing a particularly pronounced response. For the remaining half, no significant effect of chemotherapy administration was observed. These findings could reflect acknowledged heterogeneity among TNBC patient tumors, with a gene profiling-based stratification of TNBCs into several sub-types, which is translated into different responses to chemotherapies (Gupta et al., 2020; Lehmann et al., 2011). Heterogeneity was also reflected in our paradigm of implantation in the avian embryo brain parenchyma. We observed various behaviors of tumor cells depending on patients, with variable propensity of cells to widely colonize the brain tissues. In some cases, tumor cells adopted a constellation pattern, whereas in others they could form either a dense mass or display a mixed pattern. In the same line, in the developing somite, engrafted patient samples showed distinct tumor patterns, ranging from dense masses to dispersed multiple foci. Together these observations could relate to particular cancer properties revealed by the graft procedure. Interestingly too, ER+ and HER2+ tumor cells were as capable as more aggressive triple negative ones of forming tumors. This indicates that both the developing somite and the avian brain microenvironment provide effective support for tumorigenesis while also allowing heterogeneity between patients to be manifested.

Our data with ASNase supports the relevance of using of our approach for preclinical investigation. Anti-tumor efficacy was demonstrated for ASNase in both the MDA-MB-436 TNBC cell line and patient biopsies, and suited for evaluating both therapeutic compounds at different doses and combination therapies. This key preclinical finding strongly substantiates the case for advancing ASNase therapies to TNBC clinical trials, and provided a rationale for the ongoing study in metastatic TNBC, in which eryaspase (ASNase encapsulated in red blood cells) is evaluated in combination with gemcitabine and carboplatin (NCT03674242).

Altogether, these findings establish our *in vivo* model of tumoral cell implantation in targeted regions of the avian embryo as a model of choice for preclinical investigations, conveniently integrating patient stratification in the therapeutic efficacy evaluation process, which is a major asset for the advancement to clinical trials. Furthermore, coupling the generation of patient tumor replicas to large-scale molecular analysis will open new avenues for the characterization of mechanisms of action of therapeutic compounds, the prediction of their optimal combinations, and the development of personalized medicine.

In the described setup, the embryonic immune system is still immature, not only facilitating tumor intake but also limiting assessment of immune involvement in the mechanisms that are studied. Further developments of the AVI-PDX model, to evaluate therapies targeting immune cells and to assess establishment of resistance mechanisms through longer period of treatments, will open novel avenues for preclinical investigations.

**Limitations of the study**

The effect of SOCs (gemcitabine, carboplatin) in the AVI-PDX model was characterized here in a short time course (24 h), allowing to assess the acute, immediate effect of these therapies on the tumor volume and at the transcriptomic level. Working on more long-term effects or emergence of mechanisms of resistance to these therapies would require longer exposure in the avian model and associated adaptations of the protocols. Moreover, in the present study we did not assess the impact of therapeutic compounds on the avian microenvironment of the tumors. It would be interesting to characterize, in more precise experiments, the transcriptomic adaptations of avian contingents to both the engrafted tumor cells and the different therapies injected.

**STAR★METHODS**

Detailed methods are provided in the online version of this paper and include the following:

- KEY RESOURCES TABLE
- RESOURCE AVAILABILITY
  - Lead contact
  - Material availability
  - Data and code availability
- EXPERIMENTAL MODEL AND SUBJECT DETAILS
  - Chick embryos
  - Cell lines
  - Patient samples
- METHOD DETAILS
  - Anticancer drugs
  - *In vitro* cell survival assay
  - *In ovo* xenografts
  - Histological staining of paraffin sections
  - Evaluation of drug toxicity in chick embryos
  - Immunofluorescence on cryosections
  - Tissue clearing and whole mount SPIM imaging
  - Concentration of plasma amino-acids by HPLC
  - RNA isolation and library preparation for high-throughput mRNA sequencing (RNA-seq)
- QUANTIFICATION AND STATISTICAL ANALYSIS

## SUPPLEMENTAL INFORMATION

Supplemental information can be found online at <https://doi.org/10.1016/j.isci.2021.103423>.

## ACKNOWLEDGMENTS

We thank Alexander Scheer, Françoise Horand, Marie Châlons-Cottavoz, and Bastien Laperrousaz for helpful discussions; Priscillia Rebus and Florian Tavernier for *in vitro* experiments performed at Erytech Pharma; Oncodesign SAS for the sharing of TNBC samples from their PDX murine models and associated clinical information; and ProfileXpert for providing advice on RNA-seq data analysis. We thank Dr. O. Derbel (Jean Mermoz Hospital, Lyon, France) and Dr. P. Chabert (Hospices Civils de Lyon, France) for their help in the management of patient TNBC samples. We thank Dr. David Meyronnet and Iris Couderc-Enguiale for histological analyses (Centre de Pathologie Et Neuropathologie Est, Hospices Civils de Lyon, France). We thank Gil Beyen, Iman El-Hariri, Dan Cole, Chad Kitchen, Nigel Biswas-Baldwin (from Erytech), and Sabine Poppenborg (from medac GmbH) for the review of this article and their useful advice. Academic work by C.D.-B. and V.C. was conducted within the frame of the LabEx CORTEX and DEVWECAN of Université de Lyon, within the program "Investissements d'Avenir" (ANR-11-IDEX-0007) operated by the French National Research Agency (ANR).

## AUTHOR CONTRIBUTIONS

L.J. and C.C. conducted experiments involving the avian model. F. Gallix and S.C. performed *in vitro* experiments with ASNase and spectrophotometric analyses of amino acids in chick embryonic plasma. F. Gay and O.I. analyzed RNA-seq data. R.T. analyzed *in vivo* data and participated to the revisions of the manuscript. E.M. provided and characterized murine PDX samples. K.A. conceived experiments related to ASNase and wrote the related sections of the paper. C.D.-B. and V.C. conceived the experiments, analyzed data related to the avian model, and wrote the paper.

## DECLARATION OF INTERESTS

V.C. and C.D.-B. are co-founders of OncoFactory SAS ([www.oncofactory.com](http://www.oncofactory.com)). L.J., C.C., and R.T. are employees of OncoFactory SAS. F. Gallix, S.C., F. Gay, and K.A. are employees of Erytech Pharma. This work is related to the international patent WO2017/103,025.

Received: April 13, 2021

Revised: September 30, 2021

Accepted: November 8, 2021

Published: December 17, 2021

**REFERENCES**

- Ahlike, E., Nowak-Göttl, U., Schulze-Westhoff, P., Werber, G., Börste, H., Würthwein, G., Jürgens, H., and Boos, J. (1997). Dose reduction of asparaginase under pharmacokinetic and pharmacodynamic control during induction therapy in children with acute lymphoblastic leukaemia. *Br. J. Haematol.* 96, 675–681. <https://doi.org/10.1046/j.1365-2141.1997.d01-2089.x>.
- Berti, F., Nogueira, J.M., Wöhrle, S., Sobreira, D.R., Hawrot, K., and Dietrich, S. (2015). Time course and side-by-side analysis of mesodermal, pre-myogenic, myogenic and differentiated cell markers in the chicken model for skeletal muscle formation. *J. Anat.* 227, 361–382. <https://doi.org/10.1111/joa.12353>.
- Clézardin, P., Coleman, R., Puppo, M., Ottewill, P., Bonnellye, E., Paycha, F., Confavreux, C.B., and Hohen, I. (2021). Bone metastasis: Mechanisms, therapies, and biomarkers. *Physiol. Rev.* 101, 797–855. <https://doi.org/10.1152/physrev.00012.2019>.
- Coniglio, S.J. (2018). Role of tumor-derived chemokines in osteolytic bone metastasis. *Front. Endocrinol.* 9, 313. <https://doi.org/10.3389/fendo.2018.00313>.
- Coussy, F., de Koning, L., Lavigne, M., Bernard, V., Ouine, B., Boulai, A., El Botty, R., Dahmani, A., Montaudon, E., Assayag, F., et al. (2019). A large collection of integrated genomically characterized patient-derived xenografts highlighting the heterogeneity of triple-negative breast cancer. *Int. J. Cancer* 145, 1902–1912. <https://doi.org/10.1002/ijc.32266>.
- Delloye-Bourgeois, C., Bertin, L., Thoinet, K., Jarrosson, L., Kindbeiter, K., Buffet, T., Tauszig-Delamasure, S., Bozon, M., Marabelle, A., Combaret, V., et al. (2017). Microenvironment-driven shift of cohesion/detachment balance within tumors induces a switch toward metastasis in neuroblastoma. *Cancer Cell* 32, 427–443.e8. <https://doi.org/10.1016/j.ccell.2017.09.006>.
- Dobrolecki, L.E., Airhart, S.D., Alferrez, D.G., Aparicio, S., Behbod, F., Bentires-Alj, M., Brisken, C., Bult, C.J., Cai, S., Clarke, R.B., et al. (2016). Patient-derived xenograft (PDX) models in basic and translational breast cancer research. *Cancer Metastasis Rev.* 35, 547–573. <https://doi.org/10.1007/s10555-016-9653-x>.
- Estlin, E.J., Ronghe, M., Burke, G.A., and Yule, S.M. (2000). The clinical and cellular pharmacology of vincristine, corticosteroids, L-asparaginase, anthracyclines and cyclophosphamide in relation to childhood acute lymphoblastic leukaemia. *Br. J. Haematol.* 110, 780–790. <https://doi.org/10.1046/j.1365-2141.2000.t01-1-02153.x>.
- Ewald, B., Sampath, D., and Plunkett, W. (2007). H2AX phosphorylation marks gemcitabine-induced stalled replication forks and their collapse upon S-phase checkpoint abrogation. *Mol. Cancer Ther.* 6, 1239–1248. <https://doi.org/10.1158/1535-7163.MCT-06-0633>.
- Graf, F., Horn, P., Ho, A.D., Boutros, M., and Maercker, C. (2021). The extracellular matrix proteins type I collagen, type III collagen, fibronectin, and laminin 421 stimulate migration of cancer cells. *FASEB J.* 35, e21692. <https://doi.org/10.1096/fj.202002558RR>.
- Gupta, G.K., Collier, A.L., Lee, D., Hoefler, R.A., Zheleva, V., Siewertsz van Reesema, L.L., Tang-Tan, A.M., Guye, M.L., Chang, D.Z., Winston, J.S., et al. (2020). Perspectives on triple-negative breast cancer: Current treatment strategies, unmet needs, and potential targets for future therapies. *Cancers* 12. <https://doi.org/10.3390/cancers12092392>.
- Hamburger, V., and Hamilton, H.L. (1992). A series of normal stages in the development of the chick embryo. *Dev. Dyn.* 195, 231–272. <https://doi.org/10.1002/aja.1001950404>.
- Hiraga, T. (2019). Bone metastasis: Interaction between cancer cells and bone microenvironment. *J. Oral Biosci.* 61, 95–98. <https://doi.org/10.1016/j.job.2019.02.002>.
- Hwang, S.-Y., Park, S., and Kwon, Y. (2019). Recent therapeutic trends and promising targets in triple negative breast cancer. *Pharmacol. Ther.* 199, 30–57. <https://doi.org/10.1016/j.pharmthera.2019.02.006>.
- Jin, G., Zhao, J., Qi, H., Lou, M., Liu, X., Qu, Y., Zhao, L., Zhang, W., Shao, J., and Zhong, H. (2013). Gemcitabine and carboplatin demonstrate synergistic cytotoxicity in cervical cancer cells by inhibiting DNA synthesis and increasing cell apoptosis. *OncoTargets Ther.* 6, 1707–1717. <https://doi.org/10.2147/OTT.S54217>.
- Kar, S., Jasuja, H., Katti, D.R., and Katti, K.S. (2020). Wnt/ $\beta$ -Catenin signaling pathway regulates osteogenesis for breast cancer bone metastasis: Experiments in an in vitro nanoclay scaffold cancer testbed. *ACS Biomater. Sci. Eng.* 6, 2600–2611. <https://doi.org/10.1021/acsbomaterials.9b00923>.
- Karginova, O., Siegel, M.B., Van Swearingen, A.E.D., Deal, A.M., Adamo, B., Sambade, M.J., Bazyar, S., Nikolaishvili-Feinberg, N., Bash, R., O’Neal, S., et al. (2015). Efficacy of carboplatin alone and in combination with ABT888 in intracranial murine models of BRCA-mutated and BRCA-wild-type triple-negative breast cancer. *Mol. Cancer Ther.* 14, 920–930. <https://doi.org/10.1158/1535-7163.MCT-14-0474>.
- Kawaguchi, N., Zhang, T.-T., and Nakanishi, T. (2019). Involvement of CXCR4 in normal and abnormal development. *Cells* 8. <https://doi.org/10.3390/cells8020185>.
- Klingberg, A., Hasenberg, A., Ludwig-Portugall, I., Medyukhina, A., Männ, L., Brenzel, A., Engel, D.R., Figge, M.T., Kurts, C., and Gunzer, M. (2017). Fully automated evaluation of total glomerular number and capillary tuft size in nephritic kidneys using lightsheet microscopy. *J. Am. Soc. Nephrol.* 28, 452–459. <https://doi.org/10.1681/ASN.2016020232>.
- Larsson, P., Engqvist, H., Biermann, J., Werner Rönnerman, E., Forssell-Aronsson, E., Kovács, A., Karlsson, P., Helou, K., and Parris, T.Z. (2020). Optimization of cell viability assays to improve replicability and reproducibility of cancer drug sensitivity screens. *Sci. Rep.* 10, 5798. <https://doi.org/10.1038/s41598-020-62848-5>.
- Lehmann, B.D., Bauer, J.A., Chen, X., Sanders, M.E., Chakravarthy, A.B., Shyr, Y., and Pietenpol, J.A. (2011). Identification of human triple-negative breast cancer subtypes and preclinical models for selection of targeted therapies. *J. Clin. Invest.* 121, 2750–2767. <https://doi.org/10.1172/JCI45014>.
- Maisano, R., Zavettieri, M., Azzarello, D., Raffaele, M., Maisano, M., Bottari, M., and Nardi, M. (2011). Carboplatin and gemcitabine combination in metastatic triple-negative anthracycline- and taxane-pretreated breast cancer patients: A phase II study. *J. Chemother.* 23, 40–43. <https://doi.org/10.1179/joc.2011.23.1.40>.
- Marangoni, E., Laurent, C., Coussy, F., El-Botby, R., Château-Joubert, S., Servely, J.-L., de Plater, L., Assayag, F., Dahmani, A., Montaudon, E., et al. (2018). Capecitabine efficacy is correlated with TYMP and RB1 expression in PDX established from triple-negative breast cancers. *Clin. Cancer Res.* 24, 2605–2615. <https://doi.org/10.1158/1078-0432.CCR-17-3490>.
- Marangoni, E., Vincent-Salomon, A., Auger, N., Degeorges, A., Assayag, F., de Cremoux, P., de Plater, L., Guyader, C., De Pinieux, G., Judde, J.-G., et al. (2007). A new model of patient tumor-derived breast cancer xenografts for preclinical assays. *Clin. Cancer Res.* 13, 3989–3998. <https://doi.org/10.1158/1078-0432.CCR-07-0078>.
- Maschner, A., Krück, S., Draga, M., Pröls, F., and Scaal, M. (2016). Developmental dynamics of occipital and cervical somites. *J. Anat.* 229, 601–609. <https://doi.org/10.1111/joa.12516>.
- Medina, M.A., Oza, G., Sharma, A., Arriaga, L.G., Hernández Hernández, J.M., Rotello, V.M., and Ramirez, J.T. (2020). Triple-negative breast cancer: A review of conventional and advanced therapeutic strategies. *Int. J. Environ. Res. Public Health* 17. <https://doi.org/10.3390/ijerph17062078>.
- Mehanna, J., Haddad, F.G., Eid, R., Lambertini, M., and Kourie, H.R. (2019). Triple-negative breast cancer: Current perspective on the evolving therapeutic landscape. *Int. J. Womens Health* 11, 431–437. <https://doi.org/10.2147/IJWH.S178349>.
- Mintz, R.L., Lao, Y.-H., Chi, C.-W., He, S., Li, M., Quek, C.H., Shao, D., Chen, B., Han, J., Wang, S., and Leong, K.W. (2020). CRISPR/Cas9-mediated mutagenesis to validate the synergy between PARP1 inhibition and chemotherapy in BRCA1-mutated breast cancer cells. *Bioeng. Transl. Med.* 5, e10152. <https://doi.org/10.1002/btm2.10152>.
- Mukherjee, A., Hollern, D.P., Williams, O.G., Rayburn, T.S., Byrd, W.A., Yates, C., and Jones, J.D. (2018). A review of FOXI3 regulation of development and possible roles in cancer progression and metastasis. *Front. Cell Dev. Biol.* 6, 69. <https://doi.org/10.3389/fcell.2018.00069>.
- Müller, H.J., and Boos, J. (1998). Use of L-asparaginase in childhood ALL. *Crit. Rev. Oncol. Hematol.* 28, 97–113. [https://doi.org/10.1016/s1040-8428\(98\)00015-8](https://doi.org/10.1016/s1040-8428(98)00015-8).
- Nagasawa, T., Hirota, S., Tachibana, K., Takakura, N., Nishikawa, S., Kitamura, Y., Yoshida, N., Kikutani, H., and Kishimoto, T. (1996). Defects of

B-cell lymphopoiesis and bone-marrow myelopoiesis in mice lacking the CXC chemokine PBSF/SDF-1. *Nature* 382, 635–638. <https://doi.org/10.1038/382635a0>.

Ou, J., Zhu, X., Zhang, H., Du, Y., Chen, P., Wang, J., Peng, X., Bao, S., Zhang, X., Zhang, T., and Pang, C.L.K. (2020). A retrospective study of gemcitabine and carboplatin with or without intravenous vitamin C on patients with advanced triple-negative breast cancer. *Integr. Cancer Ther.* 19, 1534735419895591. <https://doi.org/10.1177/1534735419895591>.

Park, M.K., Lee, C.H., and Lee, H. (2018). Mouse models of breast cancer in preclinical research. *Lab. Anim. Res.* 34, 160–165. <https://doi.org/10.5625/lar.2018.34.4.160>.

Plunkett, W., Huang, P., Xu, Y.Z., Heinemann, V., Grunewald, R., and Gandhi, V. (1995). Gemcitabine: Metabolism, mechanisms of action, and self-potential. *Semin. Oncol.* 22, 3–10.

Pourquié, O. (2018). Somite formation in the chicken embryo. *Int. J. Dev. Biol.* 62, 57–62. <https://doi.org/10.1387/ijdb.180036op>.

Previdi, S., Maroni, P., Matteucci, E., Broggin, M., Bendinelli, P., and Desiderio, M.A. (2010). Interaction between human-breast cancer metastasis and bone microenvironment through activated hepatocyte growth factor/Met and

beta-catenin/Wnt pathways. *Eur. J. Cancer* 46, 1679–1691. <https://doi.org/10.1016/j.ejca.2010.02.036>.

Sasaki, A., Tsunoda, Y., Tsuji, M., Udaka, Y., Oyamada, H., Tsuchiya, H., and Oguchi, K. (2014). Decreased miR-206 expression in BRCA1 wild-type triple-negative breast cancer cells after concomitant treatment with gemcitabine and a Poly(ADP-ribose) polymerase-1 inhibitor. *Anticancer Res.* 34, 4893–4897.

Scaal, M., Bonafede, A., Dathe, V., Sachs, M., Cann, G., Christ, B., and Brand-Saberi, B. (1999). SF/HGF is a mediator between limb patterning and muscle development. *Development* 126, 4885–4893.

Schoch, S., Gajewski, S., Rothfuß, J., Hartwig, A., and Köberle, B. (2020). Comparative study of the mode of action of clinically approved platinum-based chemotherapeutics. *Int. J. Mol. Sci.* 21. <https://doi.org/10.3390/ijms21186928>.

Sethi, N., and Kang, Y. (2011). Dysregulation of developmental pathways in bone metastasis. *Bone* 48, 16–22. <https://doi.org/10.1016/j.bone.2010.07.005>.

Shi, J., Li, Y., Jia, R., and Fan, X. (2020). The fidelity of cancer cells in PDX models: Characteristics, mechanism and clinical significance. *Int. J. Cancer* 146, 2078–2088. <https://doi.org/10.1002/ijc.32662>.

Stebler, J., Spieler, D., Slanchev, K., Molyneaux, K.A., Richter, U., Cojocar, V., Tarabykin, V., Wylie, C., Kessel, M., and Raz, E. (2004). Primordial germ cell migration in the chick and mouse embryo: The role of the chemokine SDF-1/CXCL12. *Dev. Biol.* 272, 351–361. <https://doi.org/10.1016/j.ydbio.2004.05.009>.

Tomás, A.R., Certal, A.C., and Rodríguez-León, J. (2011). FLRT3 as a key player on chick limb development. *Dev. Biol.* 355, 324–333. <https://doi.org/10.1016/j.ydbio.2011.04.031>.

Vagia, E., Mahalingam, D., and Cristofanilli, M. (2020). The landscape of targeted therapies in TNBC. *Cancers* 12. <https://doi.org/10.3390/cancers12040916>.

Wakefield, L.M., and Hill, C.S. (2013). Beyond TGFβ: Roles of other TGFβ superfamily members in cancer. *Nat. Rev. Cancer* 13, 328–341. <https://doi.org/10.1038/nrc3500>.

Williams, Sade, Alkhatib, Bashar, and Serra, Rosa (2019). Development of the axial skeleton and intervertebral disc. *Current topics in developmental biology* 133, 49–90. <https://doi.org/10.1016/bs.ctdb.2018.11.018>.

Ye, L., and Jiang, W.G. (2016). Bone morphogenetic proteins in tumour associated angiogenesis and implication in cancer therapies. *Cancer Lett.* 380, 586–597. <https://doi.org/10.1016/j.canlet.2015.10.036>.

STAR★METHODS

KEY RESOURCES TABLE

REAGENT or RESOURCE	SOURCE	IDENTIFIER
<b>Antibodies</b>		
Rabbit polyclonal anti-Ki67 antibody	Abcam	Cat #ab15580; RRID: AB_443209
Rat monoclonal Histone H3 (p Ser28) antibody (HTA28)	Novus	Cat #NB600-1168; RRID: AB_10002855
Mouse monoclonal anti phosphor-H2A.X (Ser139) antibody, clone JBW301	Merck-Millipore	Cat #05-636; RRID: AB_309864
Rabbit polyclonal anti-Ku80 (XRCC5) antibody	Sigma-Aldrich	Cat #K3389; RRID: AB_532311
Donkey anti-Rabbit IgG (H+L) Secondary Antibody, Alexa Fluor 555	Thermo Fisher Scientific	Cat # A31572; RRID: AB_162543
Donkey anti-Mouse IgG (H+L) Secondary Antibody, Alexa Fluor 555	Thermo Fisher Scientific	Cat # A31570; RRID: AB_2536180
FluoProbes® 547H Donkey IgG Anti-Rat IgG (H+L)	Interchim	Cat # FPSB6110; RRID: AB_
FluoProbes® 647H Donkey Anti-Mouse IgG (H+L)	Interchim	Cat # FP-SC4110; RRID: AB_2722539
<b>Biological samples</b>		
TNBC Patient sample OF-BRE-nbt219	Neurobiotec, CRB HCL, Biobank BB-033-00046, Lyon FRANCE	N/A
TNBC Patient sample OF-BRE-nbt1111	Neurobiotec, CRB HCL, Biobank BB-033-00046, Lyon FRANCE	N/A
TNBC Patient sample OF-BRE-nbt311	Neurobiotec, CRB HCL, Biobank BB-033-00046, Lyon FRANCE	N/A
TNBC Patient sample OF-BRE-nbt783	Neurobiotec, CRB HCL, Biobank BB-033-00046, Lyon FRANCE	N/A
TNBC Patient sample OF-BRE-nbt494	Neurobiotec, CRB HCL, Biobank BB-033-00046, Lyon FRANCE	N/A
TNBC Patient sample OF-BRE-001	Oncofactory's collection declared at the French Department Research (DC-2018-3275)	N/A
TNBC Patient sample OF-BRE-002	Oncofactory's collection declared at the French Department Research (DC-2018-3275)	N/A
TNBC Patient sample OF-BRE-007	Oncofactory's collection declared at the French Department Research (DC-2018-3275)	N/A
TNBC Patient sample OF-BRE-012	Oncofactory's collection declared at the French Department Research (DC-2018-3275)	N/A
TNBC Patient sample OF-BRE-016	Oncofactory's collection declared at the French Department Research (DC-2018-3275)	N/A
TNBC Patient sample OF-BRE-017	Oncofactory's collection declared at the French Department Research (DC-2018-3275)	N/A
Murine Patient-derived xenografts (PDX) OD-BRE-0503	Oncodesign, Imodi Platform	N/A
Murine Patient-derived xenografts (PDX) OD-BRE-0589	Oncodesign, Imodi Platform	N/A
Murine Patient-derived xenografts (PDX) OD-BRE-0631	Oncodesign, Imodi Platform	N/A
Murine Patient-derived xenografts (PDX) OD-BRE-0733	Oncodesign, Imodi Platform	N/A
Murine Patient-derived xenografts (PDX) HBCx-3	<a href="#">Marangoni et al., 2007, 2018; Coussy et al., 2019</a>	N/A
Murine Patient-derived xenografts (PDX) HBCx-11	<a href="#">Marangoni et al., 2007, 2018; Coussy et al., 2019</a>	N/A

(Continued on next page)

**Continued**

REAGENT or RESOURCE	SOURCE	IDENTIFIER
Murine Patient-derived xenografts (PDX) HBCx-4B	<a href="#">Marangoni et al., 2007, 2018; Coussy et al., 2019</a>	N/A
Murine Patient-derived xenografts (PDX) HBCx-10	<a href="#">Marangoni et al., 2007, 2018; Coussy et al., 2019</a>	N/A
Murine Patient-derived xenografts (PDX) HBCx-17	<a href="#">Marangoni et al., 2007, 2018; Coussy et al., 2019</a>	N/A
Murine Patient-derived xenografts (PDX) HBCx-66	<a href="#">Marangoni et al., 2007, 2018; Coussy et al., 2019</a>	N/A
Murine Patient-derived xenografts (PDX) HBCx-75	<a href="#">Marangoni et al., 2007, 2018; Coussy et al., 2019</a>	N/A

**Chemicals, peptides, and recombinant proteins**

Hoechst	Thermo Fisher Scientific	Cat# H21486
CFSE	Thermo Fisher Scientific	C34554
RPMI 1640 GlutaMAX™	Gibco	61870-010
F12 medium	Gibco	21765029
Fetal Bovine Serum (FBS)	Sigma-Aldrich	F7524
Penicillin Streptomycin	Sigma-Aldrich	P4333
Gemcitabine (100mg/ml)	Accord Healthcare	NDC 16729- 391-30
Carboplatin (10mg/ml)	Accord Healthcare	NDC 16729-295-31
L-Asparaginase	Medac GmbH	Spectrila 81021-K19 (batch: D150857C)
Ethyl Cinnamate	SIGMA	112372
Collagenase type IV	Sigma-Aldrich	C5138
Dnase I	Sigma-Aldrich	DN25
Trypsine	Sigma-Aldrich	T5266
Trypsine EDTA 0.05%	Sigma-Aldrich	T3924
PBS 1x	Gibco	14190-094
Gelatin	VWR prolabo	24360-233
Sucrose	Sigma-Aldrich	S0389
Triton 100X	Sigma-Aldrich	T9284
Bovine serum albumin	Sigma-Aldrich	A3059
Sodium Chloride 0.9% OTEC	Aguettant	600502
Dispase I	Sigma-Aldrich	D4818
HBSS (sans Ca <sup>2+</sup> /Mg <sup>2+</sup> )	Gibco	14170138

**Critical commercial assays**

Cell Counting Kit-8	SIGMA	96992
Ribo- Zero™ Gold Kit	Epicentre	MRZG126
Single Cell RNA purification kit	Norgen Bioteck	Cat.51800
SMARTer® Stranded RNA-Seq Kit	Takara-Clontech	Cat.634839
Harris Hematoxylin	RAL diagnostics	Cat#361075
Phloxine B	RAL diagnostics	Cat#350750
Safran (powder)	RAL diagnostics	Cat#369000

**Deposited data**

Raw and analyzed RNASeq Data	This paper	GSE172218
------------------------------	------------	-----------

(Continued on next page)

<b>Continued</b>		
REAGENT or RESOURCE	SOURCE	IDENTIFIER
Experimental models: Cell lines		
MDA-MB-436 TNBC	ERYTECH PHARMA, licensed from MD Anderson Cancer Center (agreement ID: OCT20-002)	RRID:CVCL_0623
Experimental models: Organisms/strains		
Embryonated eggs, naked neck strain	Couvoir de Cerveloup, Vourey, France	N/A
Software and algorithms		
Imaris 8.2.0	BitPlane	RRID:SCR_007370
Prism 8.0	GraphPad	RRID:SCR_002798
LAS X lifescience software	LEICA	RRID:SCR_013673
HTSeq count software v0.11.3	Genome Biology Unit, European Molecular Biology Laboratory, 69111 Heidelberg, Germany	RRID:SCR-013673
Toppfun gene ontology enrichment tool, Toppgene Suite	Toppgene	ToppGene Suite; <a href="https://toppgene.cchmc.org/">https://toppgene.cchmc.org/</a>
TopHat v.2.0.6.	John Hopkins University, Center for Computational Biology	RRID:SCR_013035
DEseq2 tool (3.11)	Bioconductor	RRID:SCR-015687

## RESOURCE AVAILABILITY

### Lead contact

Further information and requests for resources and reagents should be directed to and will be fulfilled by the lead contact, Valérie Castellani ([valerie.castellani@univ-lyon1.fr](mailto:valerie.castellani@univ-lyon1.fr)).

### Material availability

This study did not generate new unique reagents.

### Data and code availability

Data: bulk RNA-seq data have been deposited at GEO and are publicly available as of the date of publication. Accession number is given in the [key resources table](#).

Code: This paper does not report any original code.

Any additional information required to reanalyze the data reported in this paper is available from the lead contact upon request.

## EXPERIMENTAL MODEL AND SUBJECT DETAILS

### Chick embryos

Embryonated eggs were obtained from a local supplier (Couvoir de Cerveloup, Vourey, France). Laying hen's sanitary status was regularly checked by the supplier according to French laws. Eggs were housed in an 18°C-incubator until use. They were then incubated at 38.5°C in a humidified incubator until the desired developmental stage. In all experiments, embryos were randomized in each experimental group and were harvested at embryonic day 4 (4 days post-fertilization). The number of embryos used in each experiment is indicated in the corresponding figure.

### Cell lines

The MDA-MB-436 TNBC cell line (RRID: CVCL\_0623) was purchased by Erytech Pharma and licensed from the M.D. Anderson Cancer Center (agreement ID: OCT20-002). The cell line was cultivated in Roswell Park

Memorial Institute Medium (RPMI 1640, Gibco) supplemented with 10% Fetal Bovine Serum (FBS) and 25 U/mL Penicillin Streptomycin (Sigma).

### Patient samples

Patient samples OF-BRE-nbt219, OF-BRE-nbt1111, OF-BRE-nbt311, OF-BRE-nbt783, OF-BRE-nbt494 and associated data were obtained from NeuroBioTec (CRB HCL, Lyon France, Biobank BB-0033-00046) and are part of a collection declared at the French Department of Research (DC 2008-72).

Patient samples OF-BRE-001, OF-BRE-002, OF-BRE-007, OF-BRE-012, OF-BRE-016, OF-BRE-017 were obtained from Oncofactory's collection declared at the French Department of Research (DC-2018-3275). Patient informed consent was obtained according to French ethical rules for each sample, and collected by referent hospital practitioners (Hopital Jean Mermoz, Lyon France; Hospices Civils de Lyon, France).

Patient-Derived Xenografts (PDX) OD-BRE-0503, OD-BRE-0589, OD-BRE-0631, OD-BRE-0733 were provided by Oncodesign and established from triple negative breast cancer patient samples by Imodi platform ([www.imodi-cancer.com](http://www.imodi-cancer.com)).

Patient-Derived Xenografts (PDX) HBCx-3, HBCx-11, HBCx-4B, HBCx-10, HBCx-17, HBCx-66, HBCx-75 were established from breast cancer patients with informed consent from the patient in accordance with published protocols (Coussy et al., 2019; Marangoni et al., 2007, 2018).

All patient samples were obtained from women.

## METHOD DETAILS

### Anticancer drugs

Gemcitabine (stock solution: 100 mg/mL) and carboplatin (stock solution: 10 mg/mL) were purchased from Accord Healthcare and diluted in NaCl 0.9% for *in vivo* experiments.

L-Asparaginase (ASNase) was purchased from medac GmbH (Spectrila®, 81021-K19, batch: D150857C) and resuspended in sterile NaCl 0.9% for *in vivo* experiments.

### *In vitro* cell survival assay

For *in vitro* cytotoxicity assays, 2500 MDA-MB-436 cells were plated in 96-well plates. Treatment with increasing doses of ASNase was performed 24 hours after plating. Cell survival measurement was performed after 4 days of treatment, using a cell counting Kit-8 colorimetric assay (CCK-8 kit, Sigma, 96992). Each experiment was repeated three times. IC50 calculation was performed using Prism 8.0 (GraphPad) software.

### *In ovo* xenografts

Embryonated eggs were incubated at 38.5°C in a humidified incubator until HH14 stage. Cell lines or patient samples were dissociated and labeled with 8  $\mu$ M CFSE solution (Life Technologies). Stage HH14 chick embryos were grafted with fluorescent cells in presumptive somitic areas or in the brain parenchyma, with a glass capillary connected to a pneumatic PicoPump (PV820, World Precision Instruments) under a fluorescence stereomicroscope. Targeted tissue areas for the graft were visualized under the stereomicroscope. For cell lines, approximately 2500 living cells were grafted in each embryo, 200 to 300 for patient samples. For patient samples, the full cellular content obtained after dissociation was engrafted including stromal and/or immune cells.

### Histological staining of paraffin sections

Chick embryos were harvested and fixed in 4% buffered formalin prior to paraffin embedding, 3- $\mu$ m sectioning, and staining with hematoxylin, phloxine and saffron (HPS) according to a standard protocol. Images were captured on Zeiss Z1 Axio-observer Microscope.

### Evaluation of drug toxicity in chick embryos

Twenty-four (24) hours after drug intravenous injection, chick embryos were harvested, weighted (Sartorius Quintix35-1S) and measured along the rostro-caudal axis using Leica LASX image analysis software. The

Body Surface Area (BSA) was calculated using Dubois & Dubois formula:  $BSA (m^2) = 0.20247 \times \text{height} (m)^{0.725} \times \text{weight} (kg)^{0.425}$ .

The morphology / anatomy of each embryo was systematically analyzed to check their correct stage-related development. The criteria observed were: the survival (heart beating), the craniofacial morphology (presence of each cerebral compartment and eyes), the presence of four limb buds, the cardiac morphology, and the anatomy of embryonic annexes such as the allantois.

### Immunofluorescence on cryosections

Chick embryos were harvested and fixed in 4% Paraformaldehyde (PFA). Embryos were embedded in 7,5% gelatin- 15% sucrose in PBS to perform 20  $\mu\text{m}$  transverse cryosections. Permeabilization and saturation of sections were performed in PBS-bovine serum albumin 3%-Triton 0.5%. Anti-Ki67 (1/200, ab15580, Abcam), anti-phospho Histone H3 Ser28 (PHH3) (1/500, NB600-1168, Novus), anti-phospho-Histone H2A.X Ser139 (1/400, #05-636, Merck-Millipore, Clone JBW301), anti-Ku80 (1/100, K3389, Sigma), anti-Pax7 (1/10, DSHB) were applied to cryosections. Alexa 555 anti-rabbit IgG (1/500, A21429, Life Technologies), Alexa 555 anti-mouse IgG (1/500, A31570, Life Technologies), FluoProbes 547H donkey anti-Rat IgG (1/500, FP-SB6110, Interchim), FluoProbes 647H donkey anti-mouse IgG (1/500, FPSC4110, Interchim) were used as secondary antibody. Nuclei were stained with Hoechst (H21486, Invitrogen). Slices were imaged with a confocal microscope (Olympus, FV1000, X81) using either a 10X objective for whole slice imaging or a 40X objective to focus on Ki67 immunolabeling.

### Tissue clearing and whole mount SPIM imaging

PFA-fixed HH25 embryos were cleared using an adapted Ethyl-Cinnamate protocol (Klingberg et al., 2017). Briefly, tissues were dehydrated in ethanol successive baths finally cleared in Ethyl Cinnamate (Sigma, 112372). Cleared samples were imaged using the UltraMicroscope SPIM (LaVision Biotech). 3D-images were built using Imaris™ software. Volumetric analysis was performed using Imaris™ "Surface" module adjusted on CFSE fluorescence.

### Concentration of plasma amino-acids by HPLC

Collected blood samples underwent a centrifugation process (1000g, 4°C for 10min) to prepare plasmas. Collected supernatants (plasmas) were aliquoted and stored at -20°C until the dosage of amino acids. The determination of amino acids level (ASN, GLN, ASP, GLU) in chicken embryo plasma was performed by ion-pairing reversed-phase liquid chromatography coupled to tandem mass spectrophotometry (HPLC/MSMS) method. Chicken embryo plasma was considered depleted in ASN when concentration is < 2  $\mu\text{M}$  demonstrating the efficacy of ASNase activity (depending on doses tested).

### RNA isolation and library preparation for high-throughput mRNA sequencing (RNA-seq)

MDA-MB-436 tumors developed in chick embryos treated either gemcitabine/carboplatin or excipient were microdissected 48 hours after grafting using a stereomicroscope. Dissected tissues were dissociated using an enzymatic cocktail comprising 1.25 mg/mL Collagenase IV, 50  $\mu\text{g}/\text{mL}$  DNase and 2.9 mg/mL trypsin-EDTA. CFSE+ cells were sorted using CellenONE cell sorter (Cellenion). The experiment was performed in duplicates for each condition. The experimental design thus consisted of 4 samples divided into 2 conditions: Excipient and gemcitabine/carboplatin. RNA isolation from sorted cells and RNA-Seq processing was performed at the ProfileXpert core facility (Lyon, France). Total RNA was extracted with Norgen single cell RNA purification kit (Norgen) and the quality was checked with a Bioanalyzer 2100 (Agilent, RIN >8.0). Ribosomal RNA was depleted with Ribo-Zero™ Gold Kit (Epicentre). RNA-seq libraries were prepared with SMART-Seq@ Stranded Kit (Takara-Clontech). Samples were sequenced in wholeRNAseq using the NextSeq illumina 500 Platform (75 bp single read). Reads were mapped using TopHat v.2.1.0 against the human Genome build (hg38). Quantification was done using HTSeq-count software (0.11.3). The differential analysis was performed with the DESeq2 tool (3.11) with median of ratios normalization that allows comparison between samples.

A gene is considered to be upregulated or downregulated when its level of expression varies with a fold change greater than or equal to 1.5 between the two conditions and its adjusted p-value (padj) is less than 0.05. Transcripts with detectable expression in one condition (ON) versus no detectable expression in the other condition (OFF) were also added to the list of differentially expressed transcripts.

Analysis of main functions concerned by gene expression change was performed with ToppFun (<https://toppgene.cchmc.org/enrichment.jsp>).

#### **QUANTIFICATION AND STATISTICAL ANALYSIS**

Statistical treatment of the data was performed with Prism 8.0e (GraphPad). For parametric tests, both normality and variances homoscedasticity were checked. All statistical tests were two-sided.